Spring 2017

Investigations of PLD Grown Tungsten Oxide Thin Films

Anthony Thomas Pelton

INVESTIGATIONS OF PLD GROWN TUNGSTEN OXIDE THIN FILMS

A Masters Thesis

Presented to

The Graduate College of

Missouri State University

In Partial Fulfillment

Of the Requirements for the Degree

Master of Science, Materials Science

By

Anthony Thomas Pelton

May 2017

INVESTIGATIONS OF PLD GROWN TUNGSTEN OXIDE THIN FILMS

Physics, Astronomy, and Materials Science

Missouri State University, May 2017

Master of Science

Anthony Thomas Pelton

ABSTRACT

Pulsed laser deposition (PLD) is a promising technique for creating inexpensive, nanostructured thin films which may lead to structures suitable for photocatalysis. During this study, multiple tungsten oxide thin films were prepared using two types of PLD techniques. The first method was conducted at US Photonics, Springfield, MO, using a femtosecond laser while the second method relied on use of an excimer (nanosecond) laser located at Missouri State University. Films were first deposited on glass using both methods at room temperature. Further study was conducted on thin films deposited on sapphire and silicon deposited at room temperatures and at elevated temperatures. In addition to using two types of PLD, an investigation of the properties of tungsten oxide thin films incorporated with alkali metals was conducted. This was achieved by preparing a target using tungsten oxide with small amounts of sodium nitrate ($NaNO_3$). The addition of alkali metals has been known to change the structure as well as the electrical, chemical, and physical properties of the bulk material. After deposition, the thin films were annealed at 450°C up to 30 hours in air. Characterization of the films' structure and morphology were made using scanning electron microscopy (SEM), x-ray diffraction (XRD), Raman spectroscopy, and x-ray photoelectron spectroscopy (XPS) both before and after annealing. Characterization of the films allowed me to determine which method of PLD as well as which substrate (glass, silicon, or sapphire) is more suitable for growing thin films suitable for photocatalysis applications.

KEYWORDS: femtosecond PLD, tungsten bronzes, tungsten oxide thin films, nanosecond PLD, thin film morphology

This abstract is approved as to form and content

_____

Robert Mayanovic, PhD
Chairperson, Advisory Committee
Missouri State University

INVESTIGATIONS OF PLD GROWN TUNGSTEN OXIDE THIN FILMS

By

Anthony Thomas Pelton

A Masters Thesis
Submitted to the Graduate College
Of Missouri State University
In Partial Fulfillment of the Requirements
For the Degree of Master of Science, Materials Science

May 2017

Approved:

_____
Robert Mayanovic, PhD

_____
Kartik Ghosh, PhD

_____
Fei Wang, PhD

_____
Julie Masterson, PhD: Dean, Graduate College

ACKNOWLEDGEMENTS

I would like to thank the following individuals: Dr. Robert Mayanovic who acted as my research advisor and helped me with my research, Dr. Kartik Ghosh for the use of his lab and help with my research, Jake Conner and the U.S. Photonics team for use of their femtosecond laser, and Krishna Harsha Puppala and other graduate students for their help and support throughout my studies.

A special thanks to my sister, Tiffany Wymore, for proofreading my thesis.

Finally, I would like to dedicate my thesis to my parents, Dale and Mary Pelton. Without their support, none of this would have been possible.

TABLE OF CONTENTS

LIST OF TABLES

LIST OF FIGURES

INTRODUCTION

The pulsed laser deposition (PLD) technique is a promising approach for creating inexpensive, nanostructured thin films, and is especially useful due to its ability to deposit several different types of materials (metal oxides, nitrides, arsenides, etc.) which cannot be deposited using other available methods. A PLD system consists of a pulsed laser, vacuum chamber, substrate holder/heater, and a target holder. Ablation is achieved by hitting a target of the desired material with a high energy pulsed laser. Plasma is ejected from the material consisting of highly energetic species which travel toward a nearby substrate and condense on the surface to form a thin film.

Thin film growth can be controlled by a variety of factors including substrate temperature and chamber pressure. Due to this, film growth is usually studied at various temperatures since it is well known that substrate temperature influences the stoichiometry as well as any resultant crystallinity of the thin film.[1] Another parameter used to control film growth is chamber pressure. To control the pressure a reactive gas can be introduced to the vacuum chamber. This gas does not interfere with the intensity of the laser but it does alter the nature of the plume during ablation. Specifically, the spatial distribution of the plasma is affected by the molecules of the gas by either reaction or scattering of the species being created. Reactions within as well as the difference in the spatial distribution of the plume can result in phase transitions as well as formation of different stoichiometries of the thin film.[2]

Several of the known advantages to using PLD include the capability to produce films with complex stoichiometries as well as the ease at which one can deposit high

purity thin films with a narrow distribution of particle size.[3] The purity of the films does depend on several factors, such as the purity of any gas used, purity of the substrate, and level of the vacuum. One of the disadvantages of using nanosecond PLD (n-PLD) is the deposition of large particles on the substrate, which can be created in a variety of different ways. The two most common causes of larger particle deposition include defects on the target surface and splashing of liquid materials. Several methods for combating splashing have been investigated including one which uses a filter to allow only species with certain velocities to pass.[2] A schematic of a typical PLD chamber is shown in the diagram provided in Figure 1.1.

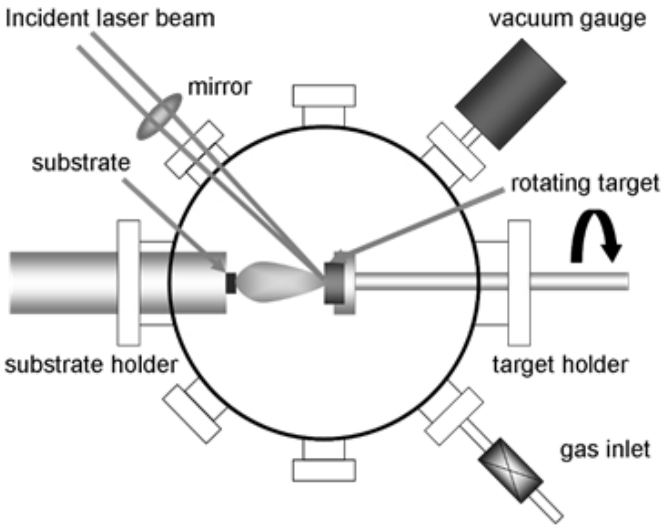

Figure 1.1: A diagram showing the PLD system.[6]

Most studies involving PLD rely on excimer or nanosecond (n) lasers. Excimer based systems use lasers with pulse lengths of the order 10^{-9} seconds and generally have wavelengths in the ultraviolet range.[4] While some studies have been made using femtosecond (f) lasers, with pulse length of the order 10^{-15} seconds and infrared

wavelengths, there is still a great deal of work to be done in this area. Since very few studies rely on use of the femtosecond PLD (f-PLD) method, the differences between films created using f-PLD and n-PLD are not well known. Using and studying this relatively new method of f-PLD to fabricate thin films helps develop the technology as well as the applications. One possible use for the f-PLD method is the production of nanostructured, thin films which are suitable for applications in photocatalysis.[5] This research attempts to help fill the gap in the understanding of the differences between both techniques and how they apply to the creation of thin films with high surface area to volume ratio structures.

Femtosecond Pulsed Laser Deposition

One difference between f-PLD and n-PLD is that films grown using n-PLD generally exhibit smooth or fine surface morphology marred by large spherical droplets.[7] An advantage of using f-PLD is the ultrashort pulse length which minimizes the number of droplets formed on the films surface[8] since f-PLD does not exhibit the same thermal effects on the target as n-PLD. The ablation process for femtosecond lasers are fundamentally different than those which arise from nanosecond lasers. When a nanosecond laser hits a target the material on the surface is melted and then evaporated by subsequent laser pulses. Here, two phase transitions (solid to melt to vapor) occur to produce a plume, while a plume is created by a direct solid to vapor transition in femtosecond pulsed laser deposition.[9] Since the femtosecond pulsed laser causes little thermal diffusion on the surface, the large particulates and smooth surfaces characteristic of n-PLD are avoided.[10]

Mechanisms by which a plasma is formed during f-PLD also differ and include several possibilities. In the case of tungsten trioxide deposition, the most likely method of ionization is multiphoton ionization which occurs when the laser intensity is very large (10^{13} W/cm^2). This process allows a bound electron to be released from the valence band when n electrons are absorbed, provided nhυ is greater than the energy band gap of an insulator or semiconductor.[11] Since the energies of the infrared photons are less than the band gap of WO_3, it will take several photons to remove the valence electrons from the atoms. Another method of ionization has been exploited by industry for several years and allows for femtosecond pulsed lasers to be useful in micromachining.[12,13] For this process to work, especially with transparent materials, a femtosecond laser must ionize electrons by the avalanche method. This method relies on free electrons ionized by the multiphoton method colliding with bound electrons until those too are ionized.[14,15]

Tungsten Oxide Thin Films as Candidate Materials

In the past, WO_3 has been used in devices such as battery electrodes,[16] gas sensors, and photo-electrochemical cells[17,18] as well as in numerous other applications. These studies were conducted using the techniques of sputtering, evaporation, chemical vapor deposition (CVD), sol-gel,[19] as well as PLD techniques.

Photocatalysis applications have been extensively studied for tungsten oxide as well as several other transition metal oxides due to their desirable band gap characteristics. Tungsten trioxide has enjoyed much of its attention due to a small, indirect bandgap of 2.4-2.8 eV which makes it active in the visible light range.[20–23] The monoclinic phase of tungsten trioxide (WO_3), has a basis of WO_6 octahedral units

resembling the cubic perovskite structure. Octahedrons are distorted from the normal MO_3 (where M is a cation) by tilting as well as a displacement of the tungsten atom from the center of the oxygen cage.[24] In this form, the octahedrons share corners as they tile together with one sheet stacked on top of another. This, tiling leads to the formation of intercalation channels between the stacks of octahedrons[25] and can be thought of as vacant sites of the monoclinic and related (orthorhombic, perovskite, etc.) structures. The monoclinic crystal system can be seen in Figure 1.2.

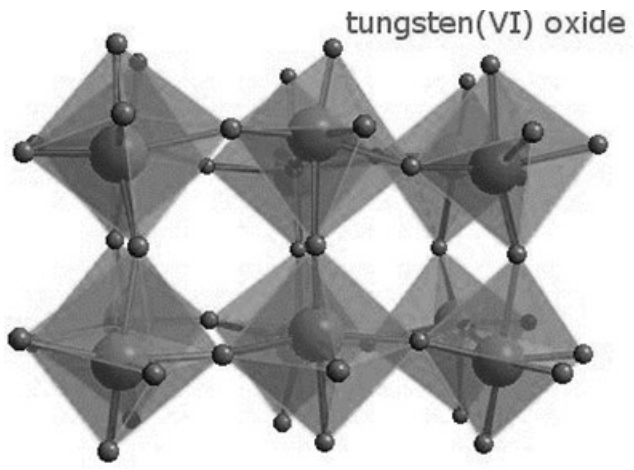

Figure 1.2: WO_6 octahedrons in a monoclinic crystal system.[27]

Tungsten trioxide can undergo several phase transitions depending on the temperature, however, these phases are usually metastable at room temperature. When ions are introduced to the vacant perovskite sites, a new chemical formula, M_xWO_3, is used to describe the structure, where M is usually an alkali ion. As the value of x increases the lattice begins to distort leading to triclinic, orthorhombic, and tetragonal phases transitions. In extreme cases (high x values), transitions to hexagonal and cubic phases are also possible.[17,19] Phase transitions caused by intercalated Na^+ ions produce

materials known as tungsten bronzes where the type of crystal structure depends on the ionic radius of the cation as well as the value of x in the formula.[26]

Annealing Effects and Substrates

While there have been many studies that have relied on various methods to synthesize tungsten trioxide thin films, one thing that remains common among these studies is the annealing temperature which most agree need to be completed at 400°C in atmosphere[28,29] to obtain the desired stoichiometry. Annealing films at this temperature not only improves the stoichiometry but also improves the crystallinity of the films.

Several substrates, and substrate temperatures, were used for deposition of tungsten trioxide based film in this study. Thin films were first deposited on glass, at room temperature, due to its easy availability. Further studies were done on films fabricated on silicon and sapphire, at room temperature and 300 °C, to determine if crystallinity of the substrate would influence film growth and surface morphology.

In the results sections of this thesis, a comparative study of tungsten trioxide thin films using the f-PLD and n-PLD methods deposited on glass will be presented along with a comparative study of tungsten trioxide thin films that have been fabricated using f-PLD deposited on both silicon and sapphire substrates. I will also discuss tungsten trioxide thin films, which have been incorporated with intercalated alkali ions, specifically sodium, known as tungsten bronzes.

EXPERIMENTAL

Target Synthesis

All targets were synthesized at Missouri State University by grinding commercially obtained WO_3 powder, using a mortar and pestle. All material was ground for at least 30 minutes to obtain powder with particles of uniform size. During the grinding process, polyvinyl alcohol (PVA) was used as a binding agent to allow cohesion of the particles. After grinding, the material was loaded into a die and pressed under 10 metric tons for several minutes to form a small cylinder with a height of 4 mm. Targets were sintered in a furnace for 12-24 hours at 800°C depending on diameter of the cylinder.

Targets containing alkali ions were synthesized in the same manner using slightly different environments for sintering. During grinding, small amounts of sodium nitrate ($NaNO_3$) were mixed with the WO_3 powder to obtain a concentration of 8at% in the target. After pressing, the targets were sintered in a furnace for 12-24 hours at 700°C depending on diameter. Lower temperatures were necessary to promote sodium incorporation since alkali ions are volatile and higher temperatures could result in evaporation.

After preparation, the targets were characterized using scanning electron microscopy (SEM), Raman spectroscopy, and x-ray diffraction (XRD). Results show that a monoclinic WO_3 target was successfully synthesized, whereas results for the Na_xWO_3 target revealed mixed phases due to non-uniform sodium incorporation. Data for these characterizations are available in the Appendix.

Pulsed Laser Deposition

Once the targets were sintered and characterized, PLD was performed using excimer and femtosecond PLD. Both the n-PLD and f-PLD systems have the same general setup but use different laser sources. Because of the differences in the lasers used in the study, several parameters including laser power and repetition rate were not the same for every run. All n-PLD runs were deposited in oxygen partial pressure while only the f-PLD runs with silicon and sapphire substrates used an oxygen environment. Table 2.1 shows some of the differences between the PLD runs done on glass which mostly focus on the differences in the type of laser used to fabricate the films.

Table 2.1: Differences in the f-PLD and n-PLD systems.

	f-PLD	n-PLD
Wavelength	775 nm	248 nm
Repetition Rate	3 kHz	10Hz
Pulse duration	120 fs	20 ns
Number of shots	1.44 million	5,000
Energy per pulse	.826 mJ	325 mJ
Chamber Pressure	10^{-5} mbar	10^{-5} mbar 10^{-4} mbar (O_2 partial pressure)
Photon Energy	1.6 eV (2.56 E-19 J)	5 eV (8.01 E-19 J)

Scanning Electron Microscopy, Helium Ion Microscopy and Energy Dispersive X-ray Spectroscopy

SEM is useful for imaging inorganic and organic samples down to the nanoscale. Images are produced which give information on the size and morphology of the thin

films. Energy dispersive x-ray spectroscopy (EDX) detectors are generally part of the SEM system and allow elemental analysis of small areas of the sample.

An SEM consists of a column, which houses the electron source and electromagnetic lenses, sample stage, and a detector. Electrons originate at the source and are accelerated down the column through the electromagnetic lenses, which are used to focus the electron beam. Once the beam hits the sample, the signal from backscattered and secondary electrons are collected by a detector and used to render an image on the screen.[30] A schematic of an SEM is shown in Figure 2.1.

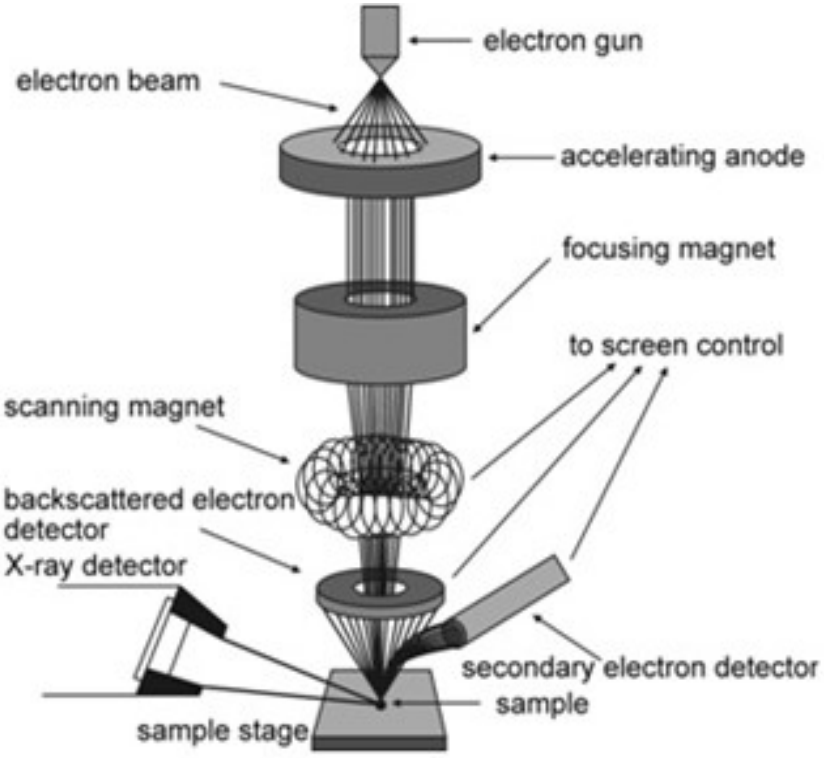

Figure 2.1: Diagram of a scanning electron microscope.[31]

The SEM located in the Physics, Astronomy, and Materials Science Department at Missouri State University (MSU) is a FEI Quanta 250. Images of the WO_3 and

Na_xWO_3 thin films were collected using an accelerating voltage of 20 kV with a working distance of approximately 10 mm and differing spot sizes. These values seem to give the best results when compared to other values for working distance and accelerating voltage. Change to: EDX was performed using the parameters indicated above.

Helium ion microscopy (HIM) is comparable to SEM apart from the particle being used. In SEM, an electron is accelerated toward the sample while in HIM a helium ion used. Several detector options are available to collect the backscattered ions and secondary electrons used as the signal. Secondary electrons are preferred for image creation due to lower noise when compared to an SEM.[32] The Zeiss Orion HIM used to image the samples in this study is located in the nanoFAB Center of the University of Alberta.

X-ray Diffraction

XRD is a useful tool in conducting complex structural analysis on crystalline samples. This tool allows for the identification of the crystal phases and the structural properties of the sample. XRD is possible because the x-rays have wavelengths measured in angstroms, which are on the same order as interatomic spacing. If the condition for diffraction, known as Bragg's law, is met then a diffraction pattern will be formed. Using the angles of the peaks the diffraction pattern, one can use Braggs law, which is given below, to determine the interatomic spacing:

$$n\lambda = 2d \sin\Theta$$

In the case of XRD, the n is equal to 1 in the above equation and the d represents the interatomic spacing. Patterns obtained from the diffractometer are given as graphs of

intensity vs 2Θ. Since the Bragg equation requires Θ, this can be obtained by simply taking half of 2Θ.[3] Figure 2.2 shows a diagram of an XRD which illustrates the Θ - 2Θ geometry of the machine.

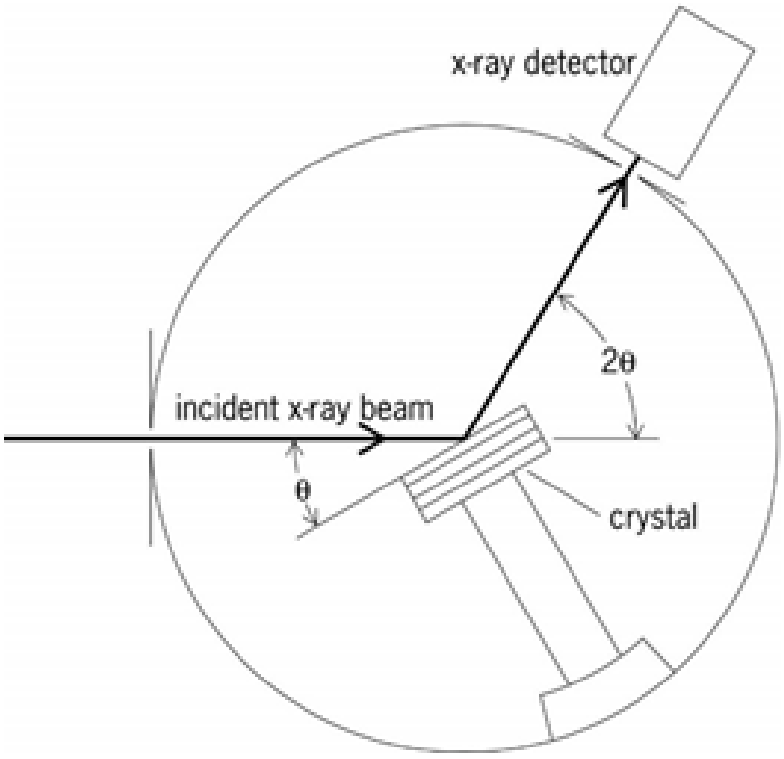

Figure 2.2: Geometry of an x-ray diffractometer.[33]

Missouri State University has a Bruker Discover D8 x-ray diffractometer which utilizes a copper source to emit Cu K_α x-rays with a wavelength of 1.5418 angstroms by using a power source of 40 kV and 40 mA. Depending on the sample, different angle range values and accumulation times were used. For tungsten bronze samples, the scans were started around 10° since diffraction peaks at lower angles are possible due to the incorporation of sodium in the structure. However, for the tungsten oxide thin films scans

were started around 15° due to proximity of the monoclinic peak that is characteristic of this material.

Raman Spectroscopy

Raman spectroscopy is a useful characterization device for providing information on the vibrational modes of atoms. When monochromatic light hits a Raman active sample it creates a dipole moment within. There are three frequencies which can be induced in the sample. One frequency corresponds to the frequency of the light source being used and is known as Rayleigh scattering. The other two slightly shifted frequencies (with respect the main line) are known as Stokes and anti-Stokes scattering bands. In Raman scattering, an electron is first excited from the ground state to a virtual vibrational state through absorption of a photon stemming from the laser. In Stokes scattering, the excited electron in the virtual state experiences a de-excitation into an excited vibrational state by releasing a photon with less energy than the photon responsible for excitation. During anti-Stokes scattering, an electron is already in an excited vibrational state when an incoming photon excites it into a virtual state. Upon de-excitation it drops into the ground state and releases a photon with more energy than the photon absorbed during excitation.[34] Figure 2.3 below illustrates the different types of Raman scattering which can occur.

Raman spectroscopy at Missouri State University is conducted on a Horiba Labram Raman-PL system. Samples were characterized using a laser with a 532 nm wavelength from approximately 100 to 1000 cm^{-1}. Accumulation time and the number of

scans to average varied with sample since some samples required longer times to collect a Raman spectrum having sufficiently high signal-to-noise ratio.

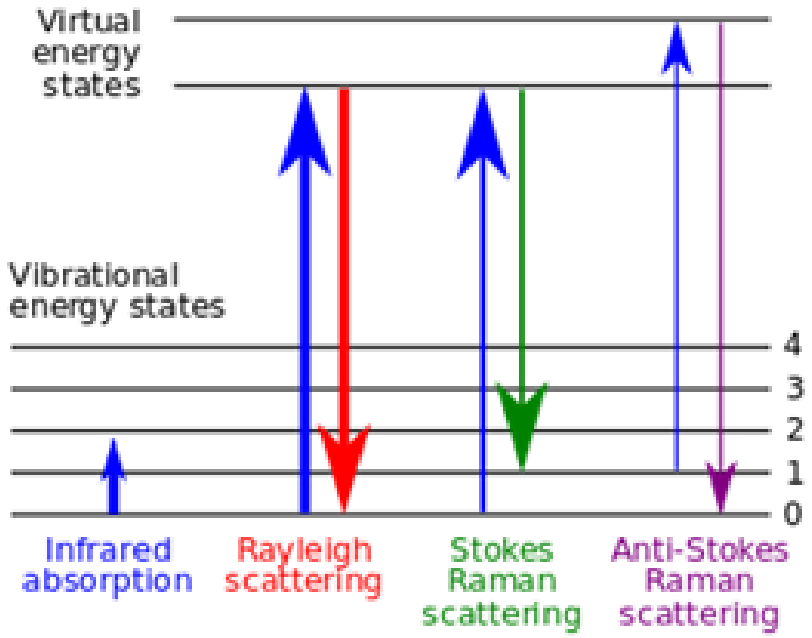

Figure 2.3: The three types of Raman scattering.[35]

X-ray Photoelectron Spectroscopy

X-ray photoelectron spectroscopy (XPS) is a surface characterization technique which is used to determine the elemental composition, empirical formula, chemical, and oxidation states of the elements that constitute the material. Characterization using XPS involves placing a sample under ultra-high vacuum and exposing the material to x-rays of a certain energy. Atoms at the surface of the material exhibit a binding potential which makes them more reactive than the atoms in the bulk of the sample. When these surface atoms are struck by the x-rays, photons are absorbed by the core electrons causing excitation, thus allowing photo electrons to break away from the nuclear attraction force

of the atom. Photo electrons are collected by a detector and have a distinct binding energy depending on the atom they are emitted from.[36] Below in figure 2.4 a schematic of the XPS machine set up is available.

Missouri State University has access to an XPS system through the Jordan Valley Innovation Center. Here the samples are placed under ultra-high vacuum and analyzed using an aluminum source utilizing the Al K_α emission at 1.486 keV. After the films were characterized using XPS, the resultant spectra were analyzed using the CASA XPS software.

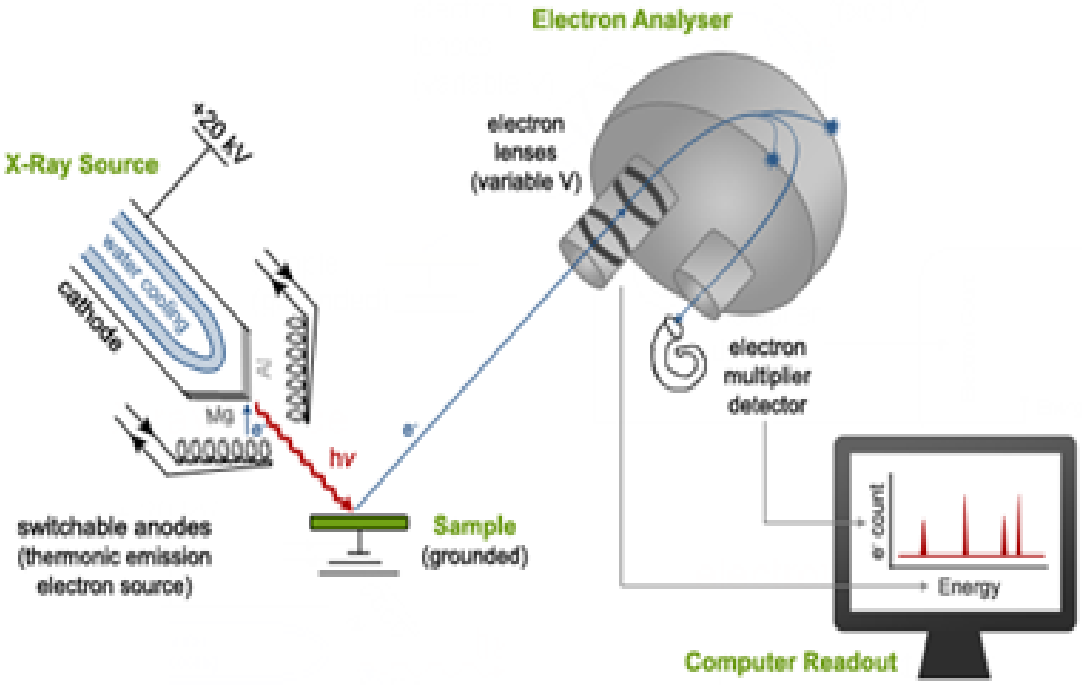

Figure 2.4: Schematic for an x-ray photoelectron spectroscopy system.[37]

Atomic Force Microscopy

Atomic force microscopy (AFM) uses a sharp, oscillating tip attached to the end of a cantilever arm to make an image of the sample surface. When the tip approaches the

surface, it experiences attractive forces which move the cantilever downward, however, as the tip comes closer to the surface repulsive forces eventually dominate and move the cantilever upward. Signal is collected using a laser and a photodiode split into four quadrants (Figure 2.5). As the cantilever moves, the laser changes position on the photodiode and the signal gathered from this procedure is used to create an image of the sample surface. After characterization, separate software is used for analysis of the AFM images. AFM analysis is useful for determining surface roughness, while the images themselves are useful for determining the 3-dimensional surface morphology of the sample.[38] Figure 2.5 show a simplified view of an AFM setup.

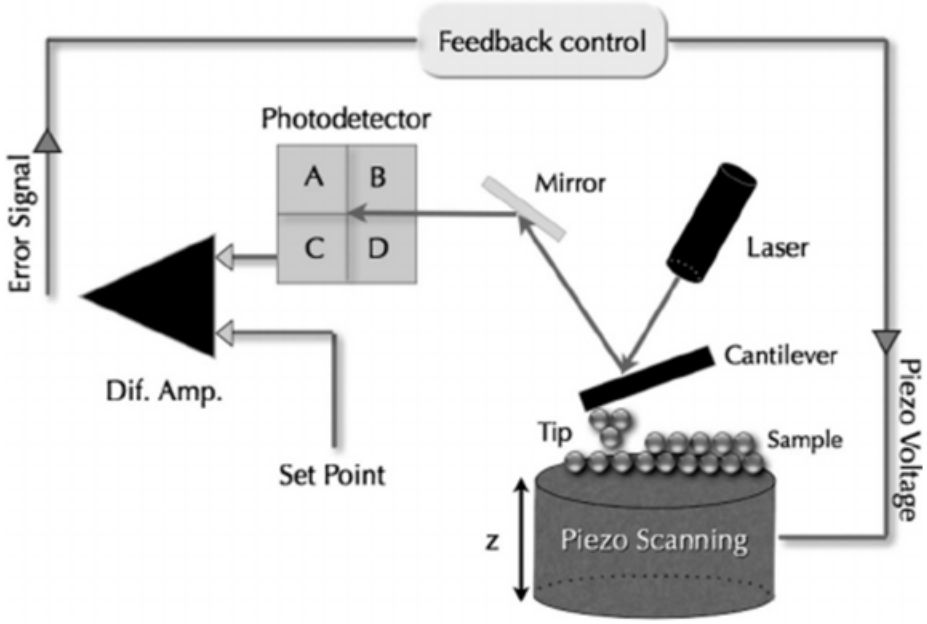

Figure 2.5: Visual description of how an atomic force microscope operates.[39]

RESULTS AND DISCUSSION

Here I will discuss the results obtained from films grown on glass, sapphire (Al_2O_3), and silicon (Si) substrates, which were held at either room temperature or at elevated temperature during deposition. First I will focus on the films which were deposited on glass using either the f-PLD or n-PLD technique to grow the films at room temperature. Thereafter, I will discuss my findings from study of tungsten oxide thin films grown on sapphire and silicon substrates that were held at either room temperature or at elevated temperature during deposition: These later films were all grown using the f-PLD technique. All the films were characterized prior to annealing as well as post annealing.

Tungsten Oxide Thin Films Grown on Glass Substrates

Three films were deposited on glass and annealed to 450 °C using a Linkam temperature controlled microscope stage when available. Annealing times varied by deposition method; the femtosecond PLD film grown on glass required annealing for 12 hours, whereas the n-PLD films were annealed for 30 hours in air to improve crystallinity. Table 3.1 lists the film names as well as the sodium concentration of each film as determined using XPS high resolution scans. Two films, fP1 and nP1 (see Table 3.1 for identification of the films grown on glass substrates) were grown using a WO_3 target, while nP2 was grown using an Na_xWO_3 target synthesized with 8 at% sodium. The additional sodium content is due to sodium diffusion from the glass which will be discussed later in this section.

Table 3.1: Sodium content obtained from XPS survey scans.

Film	Short Name	Na Content (at%)
f-PLD WO_3 Pre-Anneal	fP1 Pr-A	6.00 %
f-PLD WO_3 Post-Anneal	fP1 Pt-A	15.53 %
n-PLD WO_3 Pre-Anneal	nP1 Pr-A	14.64 %
n-PLD WO_3 Post-Anneal	nP1 Pt-A	22.27 %
n-PLD Na_xWO_3 Pre-Anneal	nP2 Pr-A	17.24 %
n-PLD Na_xWO_3 Post-Anneal	nP2 Pt-A	28.80 %

Scanning Electron Microscopy, Helium Ion Microscopy and Energy Dispersive X-ray Spectroscopy of Tungsten Oxide Thin Films Grown on Glass

Micrographs of thin films fabricated using f-PLD and n-PLD, prior to and post annealing, are shown in Figure 3.1. From the images, it is immediately clear that samples produced using f-PLD have a dramatically different morphology then those produced using n-PLD. Prior to annealing, f-PLD films consist of prominent spherical structures clustered on the film surface. Upon annealing these spheres begin to crystalize producing areas with depressions as well as tower-like structures. Conversely, the surfaces of the films synthesized using n-PLD, such as the nP1 film prior to annealing shown in Figure 3.1 (c) shows a film with fine structure. After annealing, the nP1 sample shown in Figure 3.1 (d), has developed large plate-like crystals with little relief. In contrast to what is seen in the nP1 film, the nP2 film appears to have a smooth surface prior to annealing. SEM of the material after annealing reveals the structure seen in Figure 3.2 (b), due to incomplete wetting of the glass substrate by the Na_xWO_3 material.

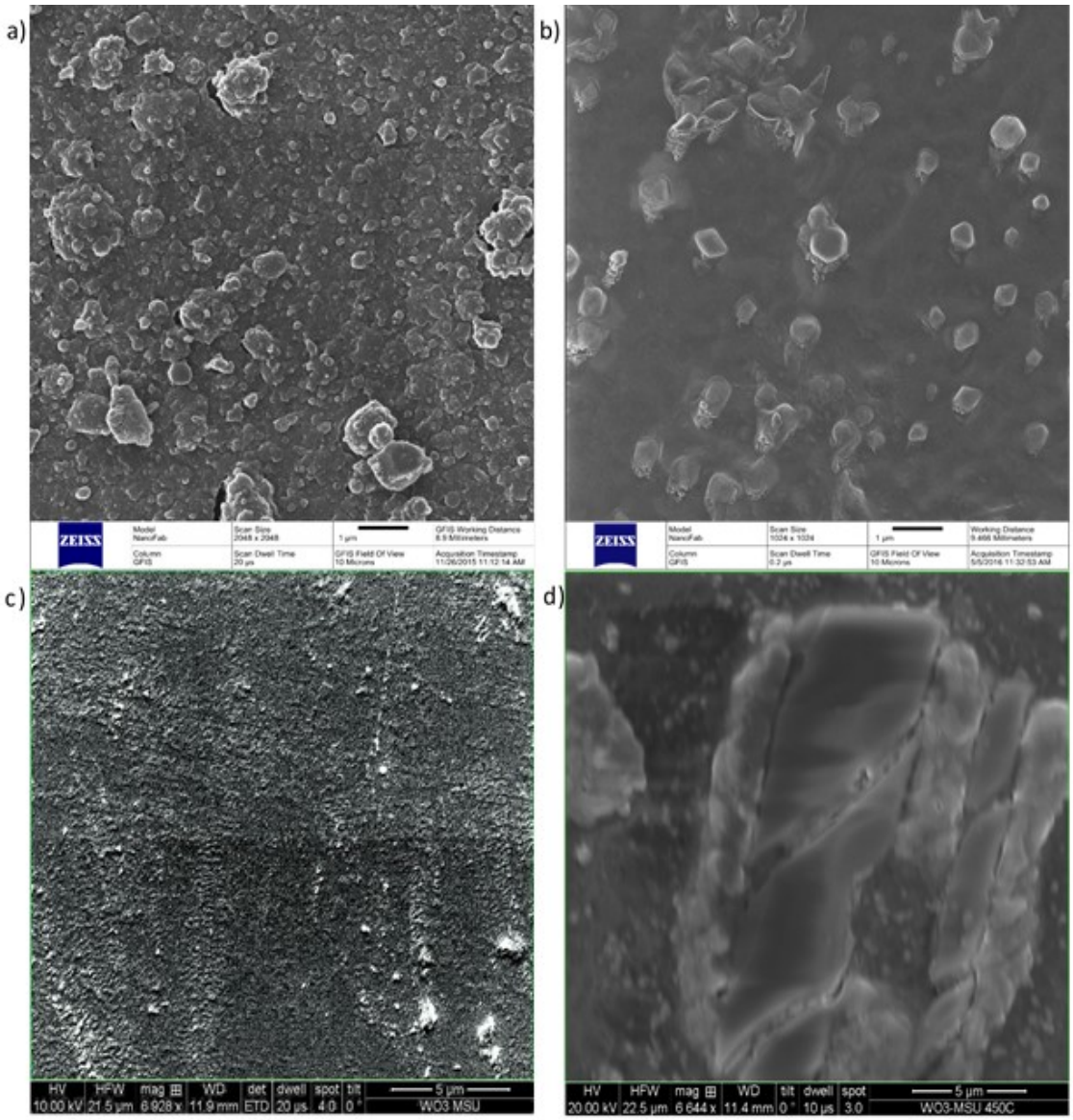

Figure 3.1: HIM of the fP1 (a) and SEM of nP1 (c) pre-annealed and fP1 (b) and nP1 (d) post-annealed films grown on glass.

Differences in the film morphology prior to annealing most likely occur due to differences in the lasers used for deposition. The high repetition rate of the femtosecond laser appears to break large spherical portions of the material off during deposition. Annealing allows these sphere-like portions to produce a 3-dimensional, nanostructured film with both low and high relief structures. During n-PLD, the nanosecond laser breaks

off very small clusters, or possibly even single ions, and propels them towards the substrate leading to the fine structure of nP1 (Figure 3.1 (c)), or the smooth structure of nP2 prior to annealing (Figure 3.2 (a)). This type of growth results in smooth films with large crystals and little 3-dimensional structures when compared to films grown using f-PLD.

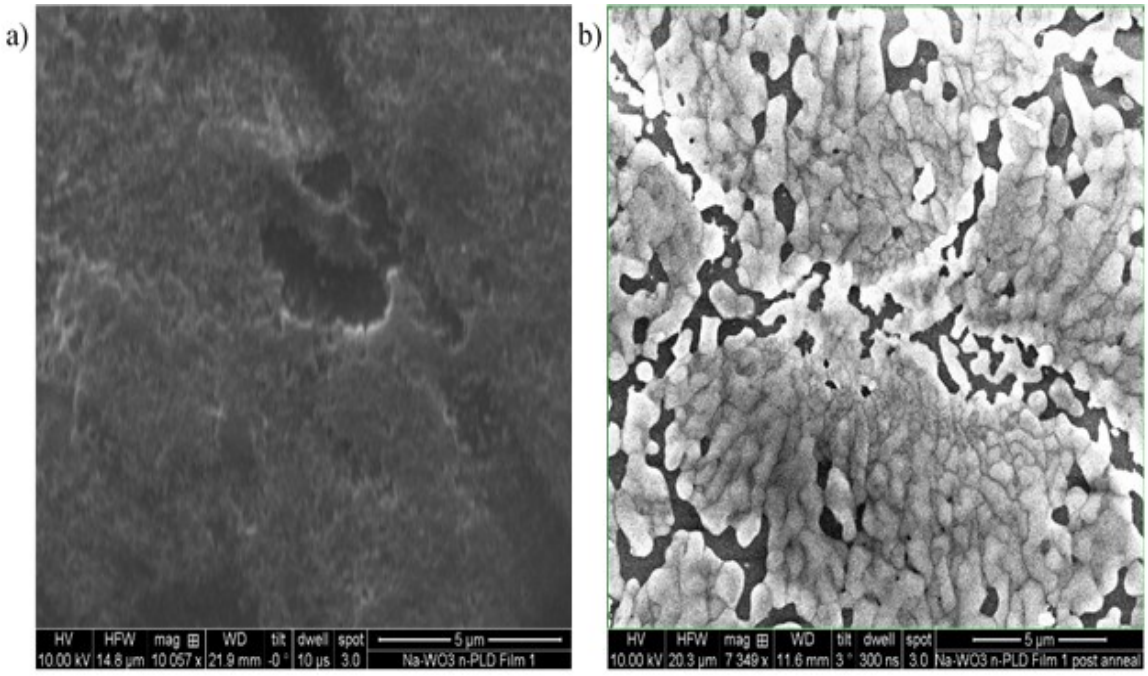

Figure 3.2: SEM of nP2 (a) pre-annealed and post-annealed (b) grown on glass.

EDX of the post annealed films confirms the presence of oxygen, sodium, and tungsten. I also see some evidence of iron in the fP1 Pt-A film as well as calcium, silicon, and potassium in the nP1 Pt-A sample. The iron is likely due to contamination during target synthesis while the calcium, silicon, and potassium are common constituents of silicate glasses. Atomic % values obtained for all the films reveal less tungsten and oxygen then the ideal WO_3 case, which are likely caused by oxygen deficiency as well as

accounting for the chemical makeup of the substrate. Figure 3.3 shows the EDX data which was obtained for these films along with a table which displays the elemental analysis from each film in both weight % and atomic %.

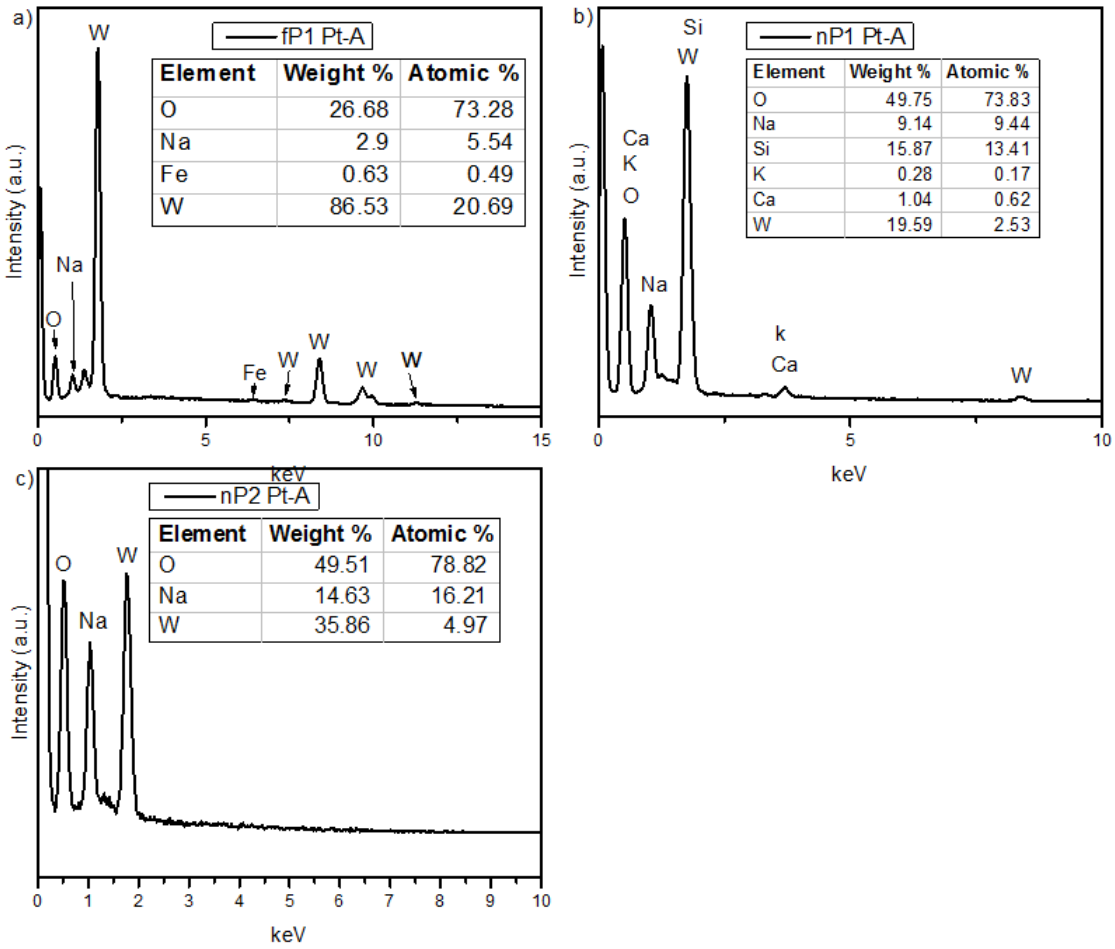

Figure 3.3: EDX data collected for the fP1 (a), nP1 (b), and nP2 (c) films after annealing.

X-ray Diffraction of Tungsten Oxide Thin Films Grown on Glass

XRD of the thin films prior to annealing revealed thin films with predominantly amorphous characteristics especially for those films grown using n-PLD. The films grown using f-PLD did appear to show slightly more aspects of crystallinity in comparison to those grown using n-PLD before annealing. Post annealing, the XRD data

showed diffraction patterns consistent with ordered materials. XRD patterns show amorphous backgrounds due to the glass slide that the sample was mounted on during characterization. Although the films should perhaps have been annealed further to ensure completely crystalline character, one can clearly see that they exhibit a high level of crystallinity.

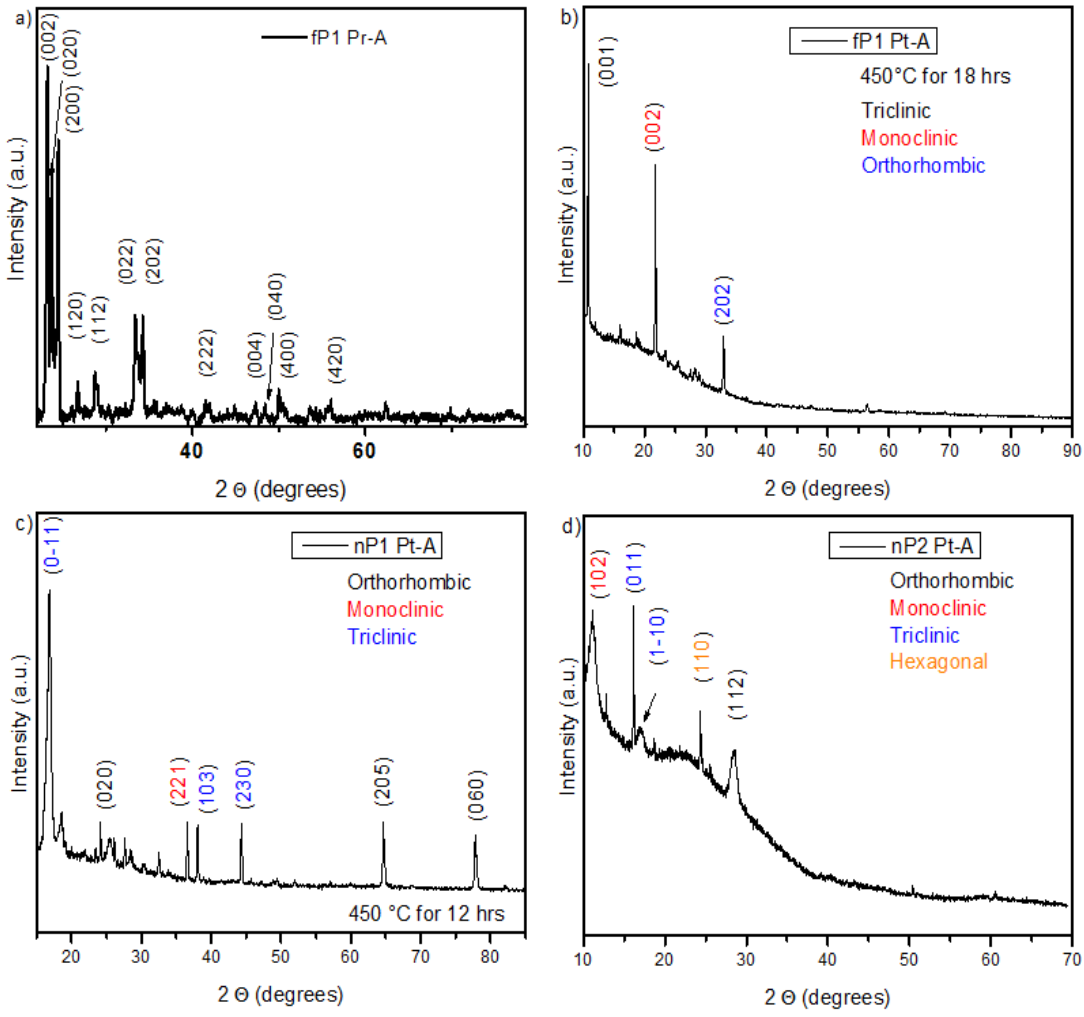

Figure 3.4: XRD for the films grown on glass: fP1 prior to annealing (a), post annealing (b), nP1 (c), and nP2 (d).

After the XRD patterns were collected they were analyzed using TOPAS version 4.2 software. Figure 3.4 below shows the XRD patterns collected from the samples on

glass. Several scans were collected and averaged for the f-PLD sample prior to annealing (Figure 3.4 (a)) which clearly shows peaks characteristic of monoclinic WO_3. However, upon closer investigation of the film after annealing (Figure 3.4 (b)) evidence supporting the presence of multiple phases is found. All films show multiple phases which are due to distortions of the WO_6 octahedrons. Distortions can be caused by two mechanisms, either sodium insertion or oxygen deficiencies which will be discussed later. Contributions from the triclinic, orthorhombic, and monoclinic phases were found in all the samples with some hexagonal aspects in the nP2 post annealed (nP2 Pt-A) sample.

Raman Spectroscopy of Tungsten Oxide Thin Films Grown on Glass

After the XRD patterns were collected, Raman spectroscopy was collected on the samples prior to and post annealing. Before annealing, Raman spectra could not be obtained for the films fabricated on glass due to their amorphous nature, which is expected due to the amorphous XRD pattern. The spectra in Figure 3.5 are for the post annealed films and will be discussed below.

After annealing, the spectra are dominated by the apical oxygen vibration modes of the WO_6 octahedron (700-810 cm^{-1} region) as well as lower frequency O-W-O bending modes in hexagonal rings of WO_6 octahedra.[40,41] The spectra obtained by Raman spectroscopy for the films after annealing can be seen in Figure 3.5. In the spectra measured from the nP2 Pt-A film, a prominent peak can be seen at approximately 940 cm^{-1} which can be attributed to W=O terminal oxygen bonds on the film surface.[42] Additional peaks in the 400-600 cm^{-1} region arise from tungsten bronze materials, due to

increased rigidity of the structure when vacant sites of the M_xWO_3 structure are filled with sodium ions.[43]

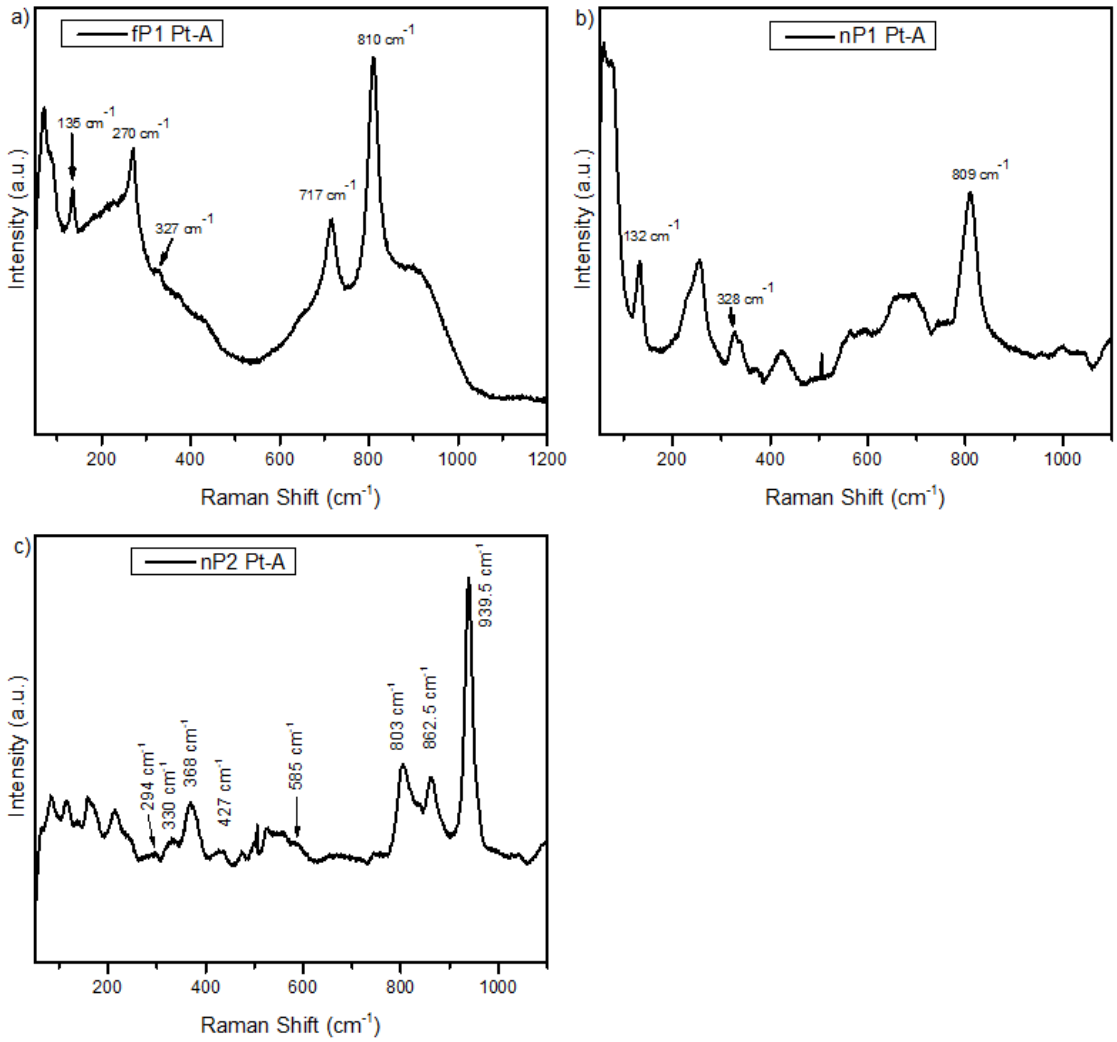

Figure 3.5: Post annealed Raman spectra of fP1 (a), nP1 (b) and nP2 (c) showing characteristic patterns of WO_3 polymorphs.

X-ray Photoelectron Spectroscopy of Tungsten Oxide Thin Films Grown on Glass

XPS high resolution spectra for fP1 Pt-A are shown in Figure 3.6. The XPS study of the films grown on glass showed that sodium was incorporated in all three films, which corresponds to the information obtained from XRD and Raman spectroscopy. The

W 4f high resolution XPS spectra of the f-PLD grown film showing the characteristic splitting of the tungsten 4f peaks and evidence for two oxidation states is the only such occurrence in this study.

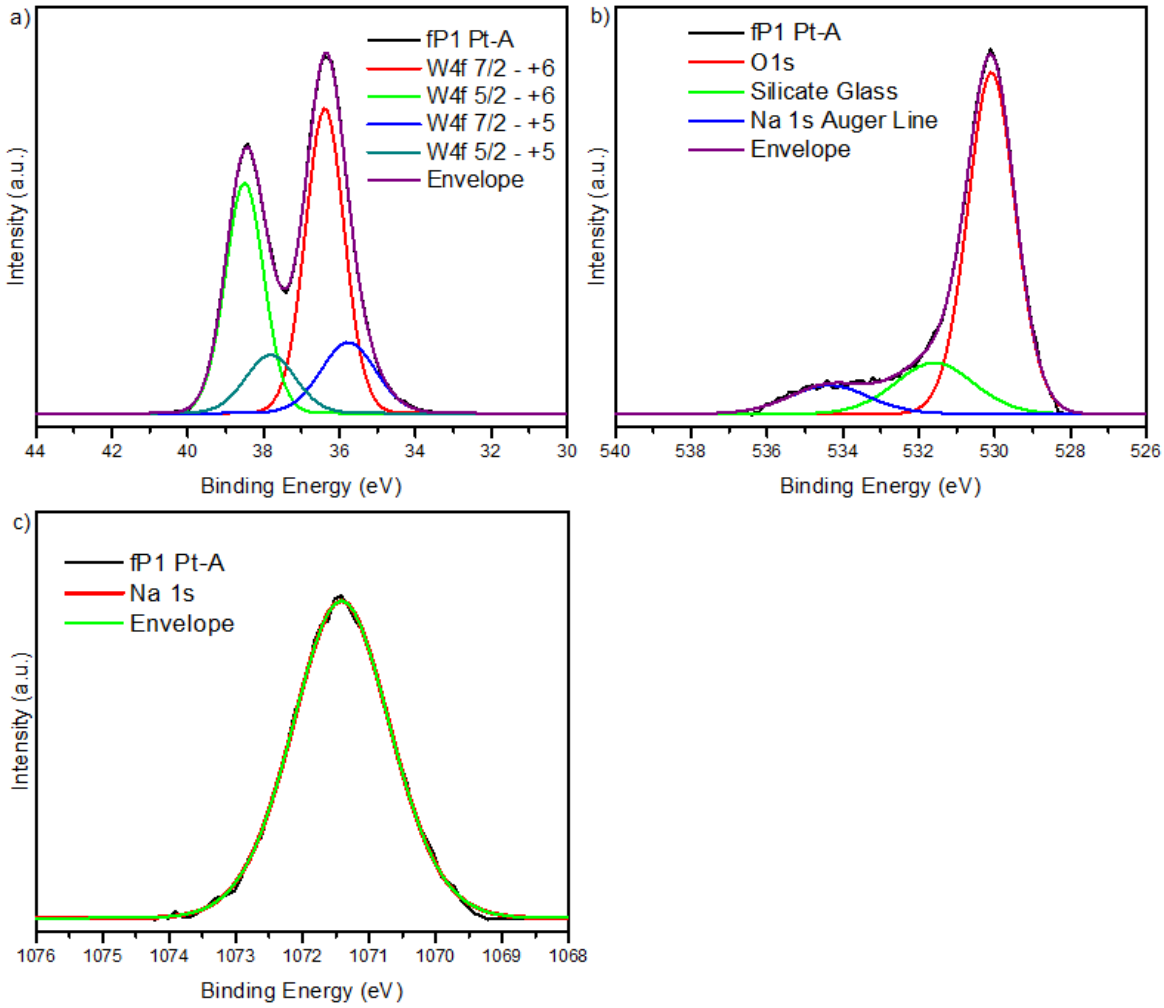

Figure 3.6: High resolution XPS of fP1 Pt-A W 4f (a), O 1s (b), and Na 1s (c).

Both the W 4f 7/2 and 5/2 peaks require two contributions for accurate fitting. The +6 contribution occurs at 35.85 and 38.07 eV for the W 4f 7/2 and 5/2 peaks, respectively, while the +5 contribution occurs at 34.77 and 37.02 eV for the W 7/2 and

5/2 peaks, respectively. These values are in good agreement with the literature and point to mixed phases in the sample.[44] The characteristic O 1s peak occurs at 530.08 eV and has a predominant W-O bonding contribution with minor contributions due to the silicate glass (531.59 eV)[45] and the Na 1s Auger line (534.37 eV). The characteristics of the nP2 Pt-A film, shown in Figure 3.7, show different features that will be discussed below.

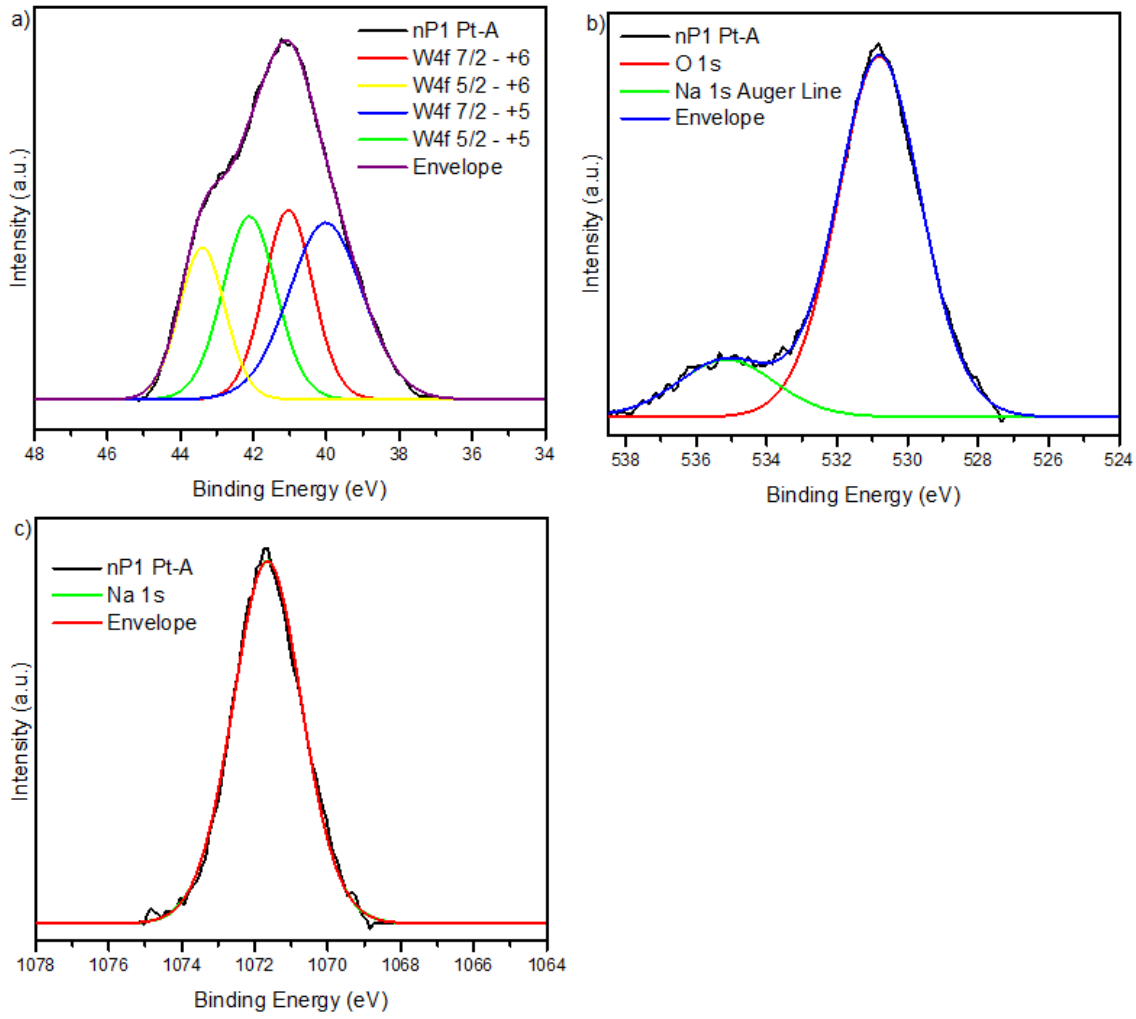

Figure 3.7. High resolution XPS of nP1 Pt-A W 4f (a), O 1s (b), and Na 1s (c).

The high-resolution XPS spectra measured from the nP1 Pt-A film are shown in Figure 3.7. The W 4f peaks in the XPS spectra measured from the n-PLD sample shows a lack of resolution in the splitting of the W 4f 7/2 and 5/2 peaks. The lack of resolution combined with a shift toward higher binding energies (approximately 5.5 eV) is characteristic of substantial incorporation of charge by the addition of the intercalated Na^+ ions. The shift in binding energy coupled with the lack of resolution of the W 4f peak indicates a change toward a tungsten bronze material.[46] The O 1s peak is clearly visible with a satellite peak on the higher binding energy side indicative of the Na 1s Auger line. Sodium 1s peaks were also seen in the sample and reveal a larger amount of sodium than in the film produced by f-PLD.

The high-resolution XPS spectra measured from the nP2 Pt-A film are shown in Figure 3.8. The case which shows the most sodium content also displays a lack of resolution in the W 4f 7/2 and 5/2 peaks along with two oxidation states. Unlike the first n-PLD film there is no shift in the W 4f peak toward higher binding energies which will need to be investigated further. One major difference is the ratio of the +5 to +6 oxidation states. In this film, the peak conforming to the +5 oxidation state contains more area than does the peak for the +6 oxidation state. This is unusual since the material used to make the target was WO_3 powder. Large sodium insertion in this film affected the ratios by allowing for more of the tungsten bronze phase to persist at room temperature. The high concentration of sodium (28.8 at%) in nP2 Pt-A is bound to change the stoicheometry of the sample (i.e., becomes non-stoichiometric phase) as well as the electrical, physical, and chemical properites.

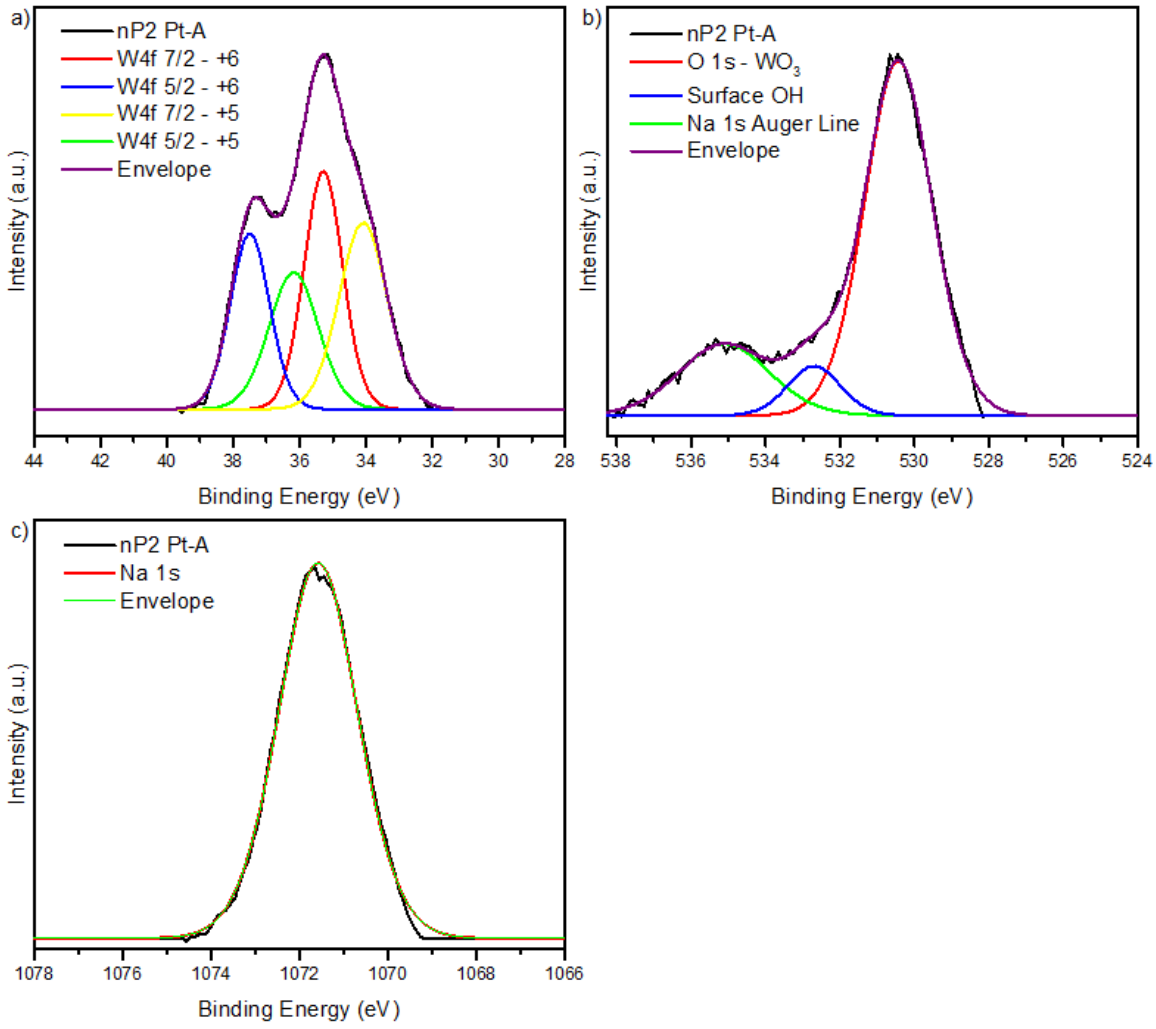

Figure 3.8: High resolution XPS of nP2 Pt-A W 4f (a), O 1s (b), and Na 1s (c).

From the XPS survey scan I determined the sodium concentration to be 6 at% for fP1 and 15.53 at% for nP1 prior to annealing. Since no sodium was incorporated into the target, the source of the sodium is by diffusion from the glass substrate during deposition and annealing. The differences in the concentration prior to annealing can be explained by considering the differences in the production of plasma by the two techniques, which is discussed below.

During the ablation process, a nanosecond laser produces a plasma by causing a solid to liquid phase transition on the target surface. With successive pulses, the target material experiences another phase transition from liquid to vapor. In a femtosecond laser, the material in a target is ablated with a direct solid to vapor phase transition. Due to these processes, the amount of kinetic energy transferred to the species inside the plasma is greater for the nanosecond laser. Since the kinetic energy is higher in the n-PLD plasma, the temperature of the plasma is greater when the material strikes the substrate, causing a relatively greater transfer of energy and increase in localized substrate temperature than for the deposition of material via f-PLD. Thus, n-PLD allows for more increased mobility of sodium ions during n-PLD than during the f-PLD process. Diffusion also occurs during annealing from the substrate leading to larger sodium concentration post annealing.

Tungsten Oxide Thin Films Grown on Sapphire and Silicon

Eight films were also deposited on sapphire (Al_2O_3) as well as silicon (Si) substrates using various target materials (WO_3 or Na_xWO_3). These films were deposited using f-PLD under oxygen partial pressure. Table 3.2 lists the parameters, such as substrate, laser poser, substrate temperature, and target materials used during deposition of the various films. Different laser power was used from one deposition to another, which is normal for the femtosecond laser since the amperage tends to drift over time. Changes in the laser power will not be discussed further since there is little evidence of differences between fP6/fP7 and fP8/fP9 films, which were grown from Na_xWO_3 targets.

Table 3.2: Information on the f-PLD films grown using sapphire and silicon substrates

Film Name	Substrate	Laser Power (W)	Shots (million)	Substrate Temp.	Target Material
fP2	Al_2O_3	2.18	1.44	300°C	WO_3
fP3	Si	2.18	1.44	300°C	WO_3
fP4	Al_2O_3	2.2	1.44	RT	WO_3
fP5	Si	2.2	1.44	RT	WO_3
fP6	Al_2O_3	1.6	1.44	RT	Na_xWO_3
fP7	Si	1.6	1.44	RT	Na_xWO_3
fP8	Al_2O_3	2.1	.9	300°C	Na_xWO_3
fP9	Si	2.1	.9	300°C	Na_xWO_3

Scanning Electron Microscopy and Energy Dispersive X-ray Spectroscopy of Tungsten Oxide Thin Films Grown on Sapphire and Silicon

Figures 3.9 shows the SEM for fP4 and fP5, while Figure 3.10 shows SEM for fP8 and fP9. Films grown on the sapphire and silicon substrates have different morphologies depending on which target is used for film growth. For instance, SEM imaging made on fP2 and fP3 show films whose surfaces primarily consist of small semi-crystalline, spherical structures. However, after annealing, these spheres give way to the tower-like structures seen on the fP1 sample. In contrast, the fP4 and fP5 films are rather smooth prior to and post annealing with little of the prominent spherical morphology seen in previous samples. It is unclear why the coverage of the fP4 and fP5 film appears to be much lower than that of the fP2 and fp3 films although the differences are likely dependent on the target since there were no major changes involving the laser during

deposition. Turning attention toward the films which were fabricated using Na_xWO_3 targets, a noticeable difference can be seen post annealing. Before and after annealing the fP6, fp7, fp8 and fp9 films show similar surface morphology as the WO_3 films. However, upon closer inspection crystals resembling small cubes and rectangles can be seen forming on the flat portions of the film, in between the tower-like structures, as well as on top of some larger crystals.

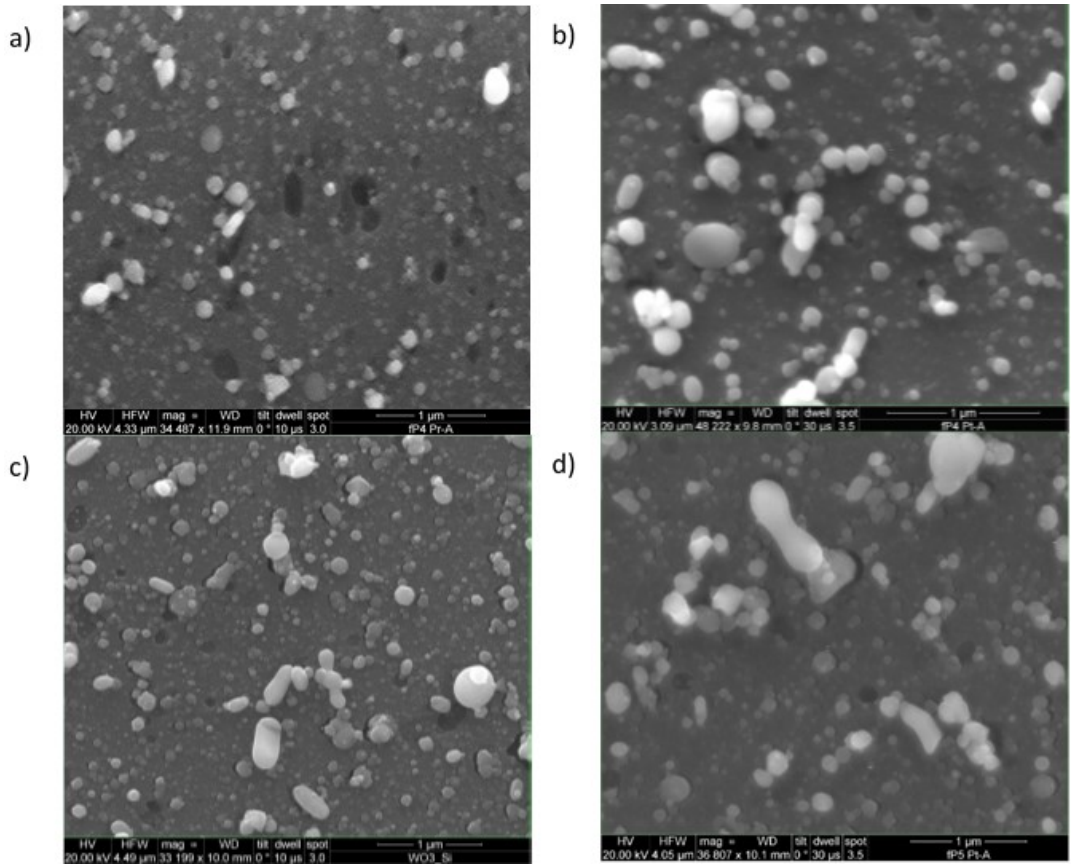

Figure 3.9: SEM of the fP4 (a) and (b) and the fP5 (c) and (d) prior to and post annealing.

While the films show similar surface morphology as grown on both sapphire and silicon substrates, more flat areas exist on the sapphire-substrate films than on the films

grown on silicon substrates. Coupled with the fact that the silicon films appear to contain more tower-like structures I can conjecture that the wettability of the WO_3 films is greater for the sapphire substrates.

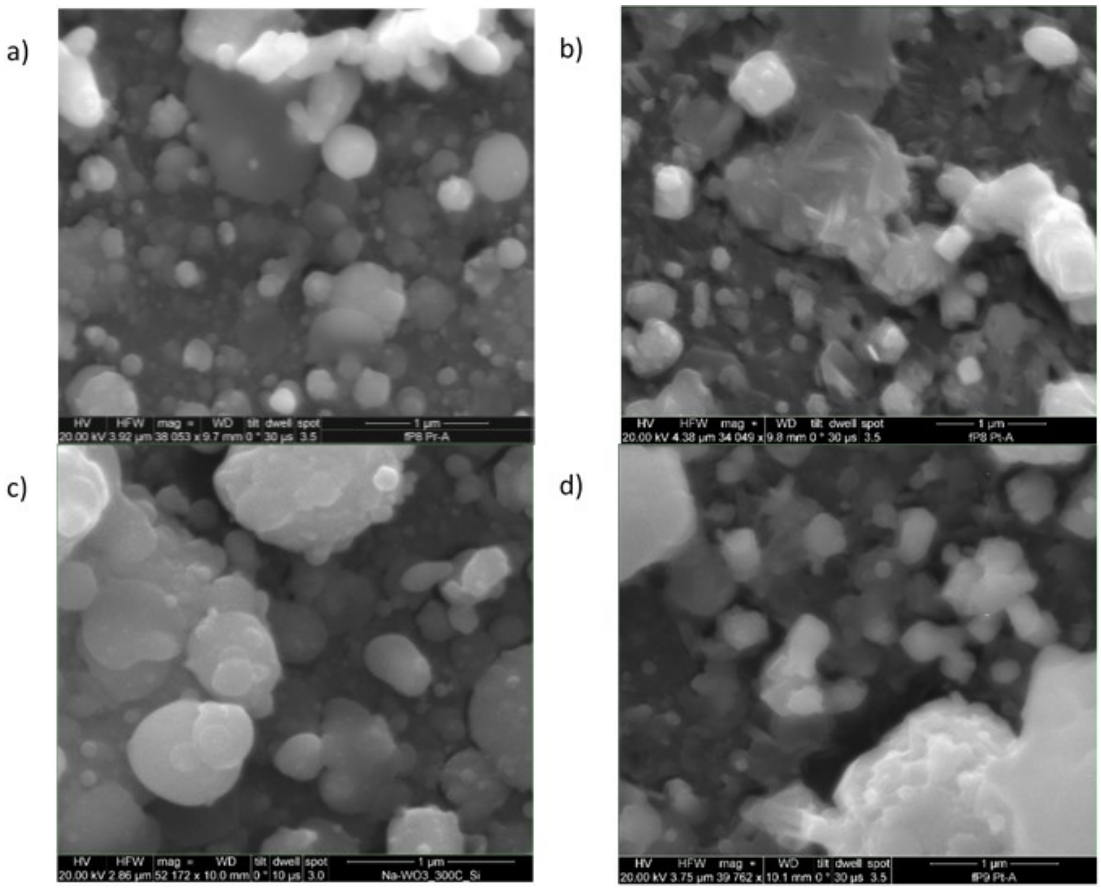

Figure 3.10: SEM for the sodium incorporated fP8 (a) and (b) and fP9 (c) and (d) films prior to and post annealing.

The EDX for fP4, fP5, fP8, and fP9 films (Figure 3.11 and Figure 3.12) show the presence of tungsten and oxygen as well as the aluminum for even numbered films and silicon for odd numbered films. I also see the presence of tungsten and oxygen on the fP6, fP7, fP8, and fP9 films with small amounts of sodium as well as the aluminum or silicon one would expect from the substrate. Some samples do show gold in the EDX

which was used to coat the samples to reduce charging effects, and the presence of calcium in the fP2 film is likely due to minor contamination due to handling of the film after deposition. Atomic percentage values are not in acceptable ranges for WO_3 which is likely due to the intense contributions from aluminum and silicon atoms from the substrates. For all other SEM and EDX results, the reader is referred to the Appendix.

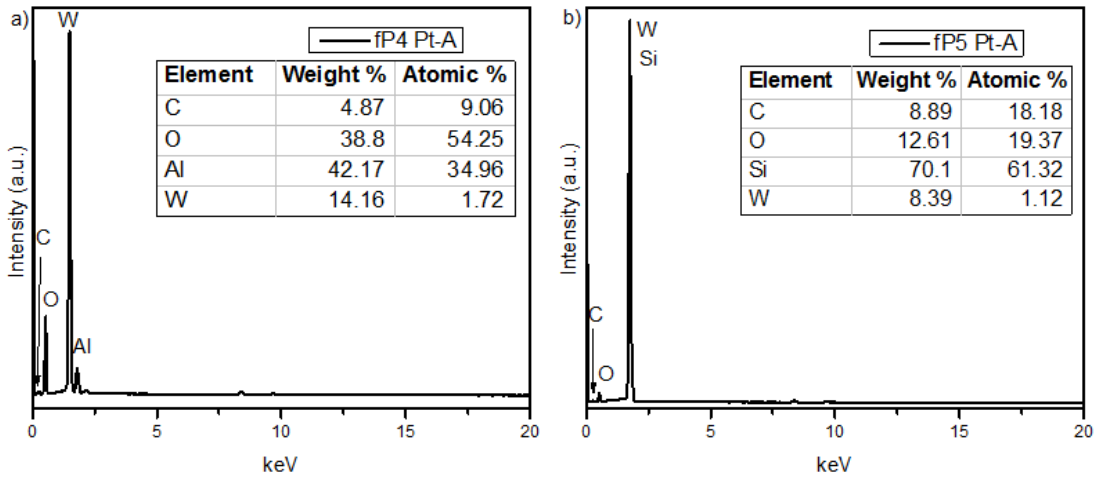

Figure 3.11: EDX of the fP4 (a) and fP5 (b) films post annealing.

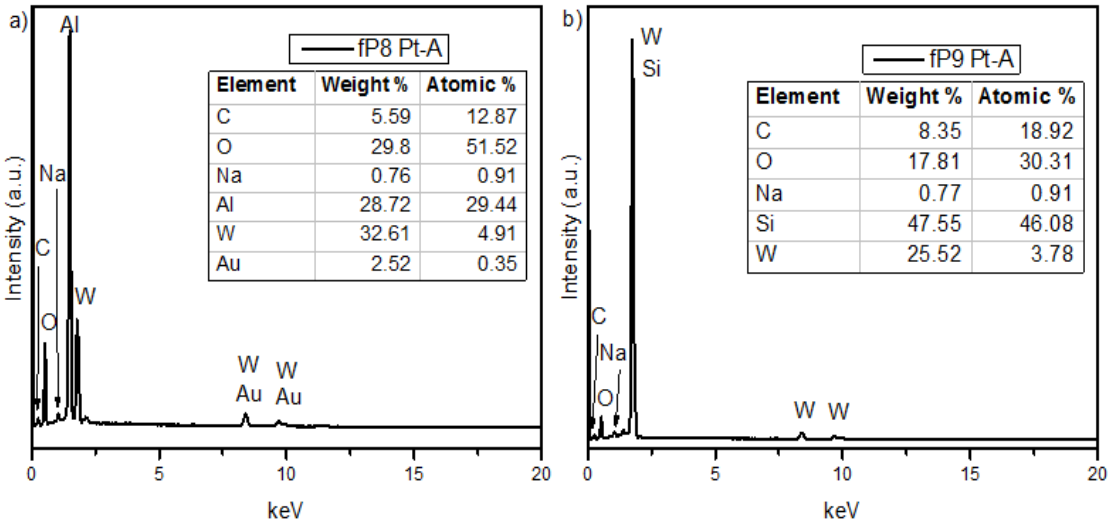

Figure 3.12: EDX collected on the fP8 (a) and fP9 (b) films post annealing.

X-ray Diffraction of Tungsten Oxide Thin Films Grown on Sapphire and Silicon

The XRD of the f-PLD films show some crystalline aspects before annealing. Prior to annealing there is a broad peak which occurs at approximately 23°, where the characteristic triple peak of the monoclinic phase is usually found. The broadening and lack of resolution of the (200), (020), and (002) peaks is likely due to the random orientation of the many semi-crystalline spheres which make up the film's surface prior to annealing. Post annealing, this broad feature begins to resolve into the monoclinic triplet while several more peaks emerge at higher 2 theta values. XRD for two of these films can be found in Figure 3.13 along with the calculated curve and some hkl values for the three most prominent phases (tetragonal, monoclinic, and orthorhombic).

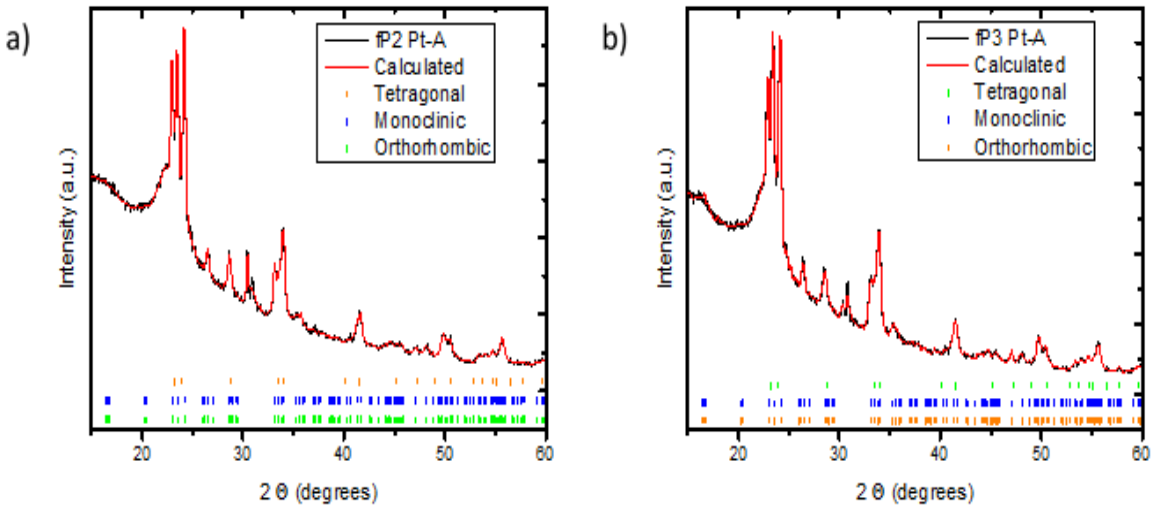

Figure 3.13: XRD for fP2 Pt-A (a) and fP3 Pt-A (b) as well as the calculated curve and hkl markers for select phases.

Reitveld refinement was carried out on the XRD patterns measured from fP2 Pt-A and fP3 Pt-A samples, which were chosen as representatives of all other samples, to determine which phases were present on the films. However, quantitative analysis of the

films will not be included due to too much variability in the percentages of phases utilized in the refinement. It was found that the samples consisted of the monoclinic, orthorhombic, tetragonal, triclinic, and hexagonal phases. Small contributions in the fP3 Pt-A sample are seen from a cubic phase. The diffraction pattern for single crystal silicon and sapphire substrates have been suppressed, due to the large intensity, by adjusting the chi stage to 7.5° and 9°, respectively. Figure 3.14 shows the XRD patterns, which were collected from all films both before and after annealing.

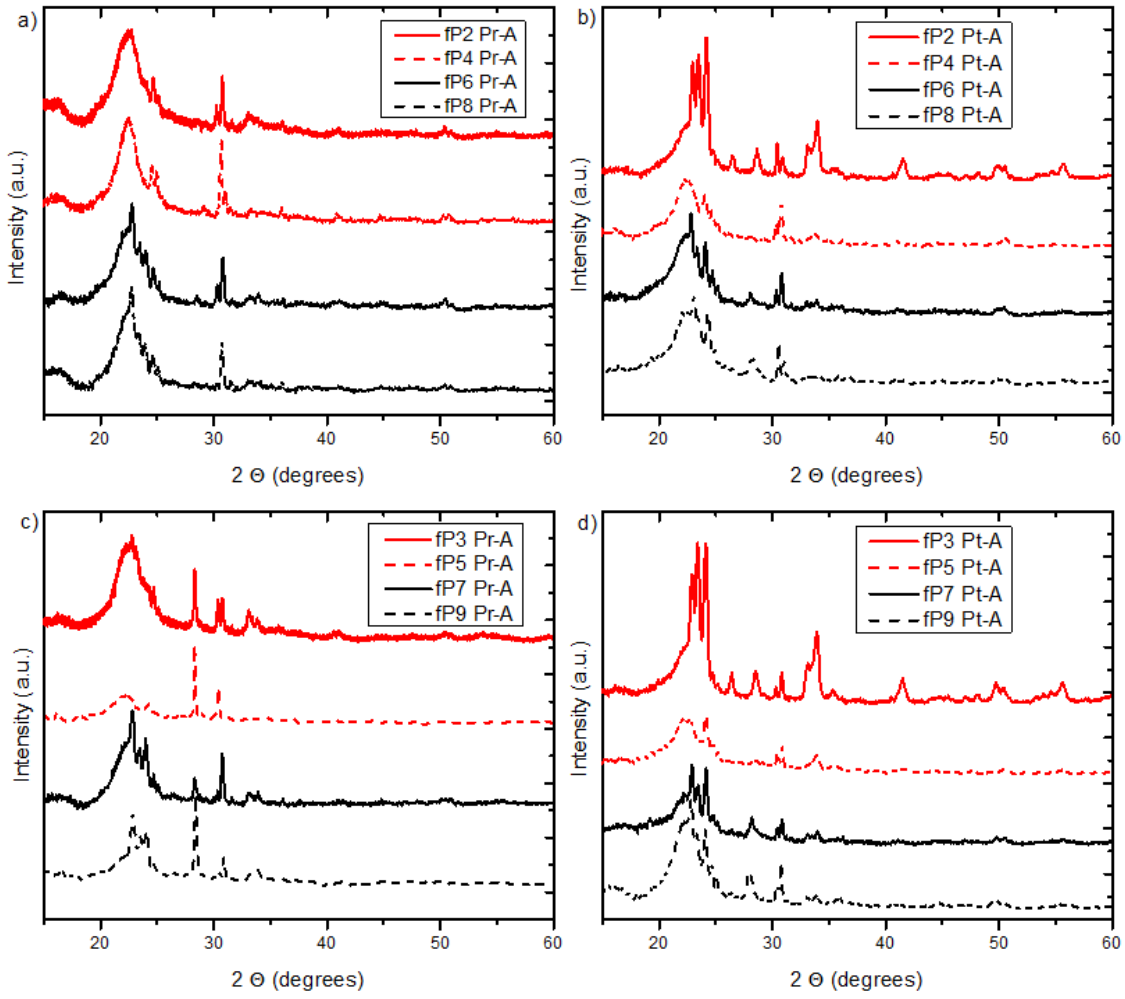

Figure 3.14 XRD for all f-PLD films grown on sapphire (a) and (b), and silicon (c) and (d)

substrates.

Raman Spectroscopy of Tungsten Oxide Thin Films Grown on Sapphire and Silicon

Raman spectra measured from all f-PLD films grown on sapphire and silicon substrates can be viewed in Figure 3.15. Raman spectroscopy obtained from the f-PLD samples show similar Raman modes as those found in the spectra for films grown on glass. Besides the apical oxygen vibration modes and the O-W-O stretching modes characteristic of WO_6 joined octahedra in the various tungsten oxide polymorphs, we also see peaks indicative of tungsten bronzes.

Since there are no alkali ions to diffuse out of the substrates, the percentage of sodium remains close to the concentration incorporated into the target. Originally, only 8 at% was added to the WO_3 target, which is relatively small when compared to the 15.53 at% of Na obtained for the fP1 Pt-A film. However, in the fP2-fP5 films, the mechanisms responsible for these new peaks in the 400 – 600 cm^{-1} are different than those in the films deposited on glass. Here, the excess phases are caused by oxygen deficiency which allows vibrational modes in the 400-600 cm^{-1} region to appear. Studies have been conducted using pulsed laser deposition which show that the crystal structure of WO_3 is affected by the oxygen partial pressure during deposition. The partial pressure used in these studies was controlled in order to produce a single crystalline phase[47,48]. The mixed phases in this study are likely due to non-uniform oxygen deficiencies caused by an inadequate oxygen partial pressure.

The yellow regions in Figure 3.15 are due to WO_3 while the peach colored regions are representative of tungsten bronze materials for fP6-fP9 films or oxygen deficiency in case of fP2-fP5 films. The additional, intense peak at approximately 520.7 cm^{-1} seen in Figure 3.15 (c) and (d) is due to Raman modes of single crystal silicon.

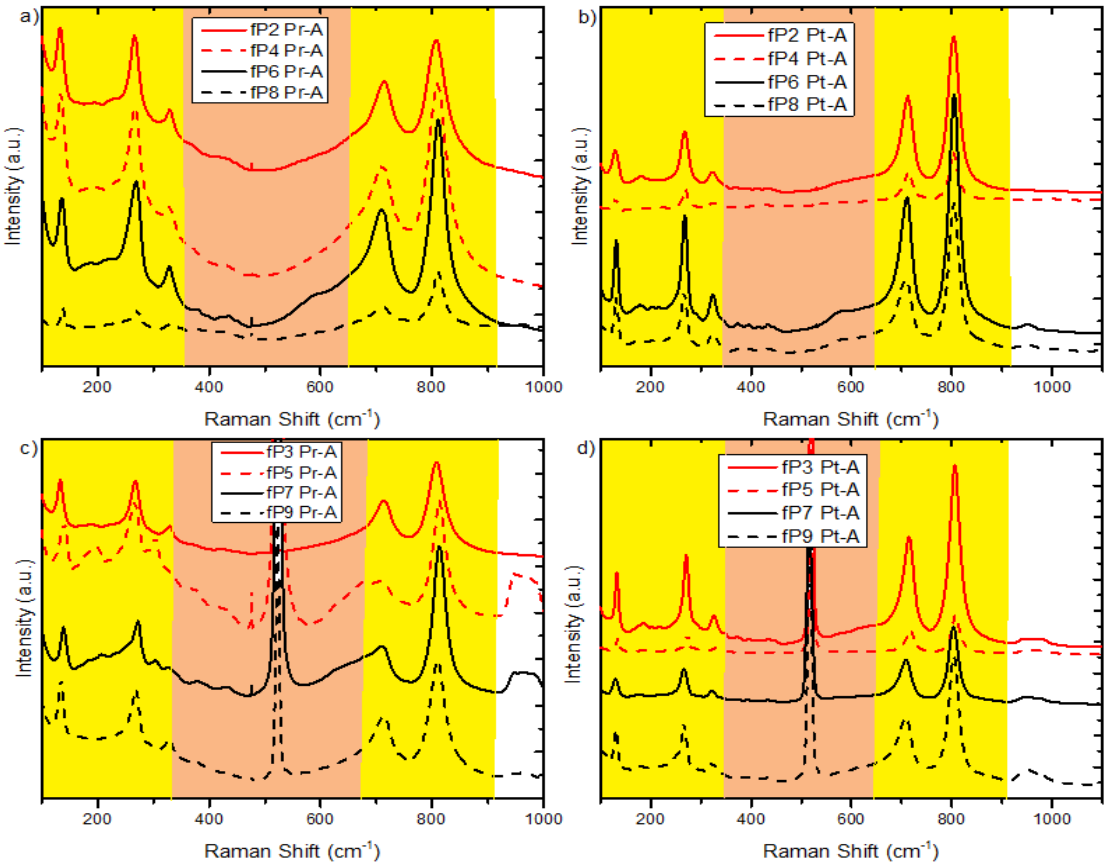

Figure 3.15: Raman spectroscopy taken from films on sapphire (a) and (b), and silicon (c) and (d) prior to and post annealing.

X-ray Photoelectron Spectroscopy of Tungsten Oxide Thin Films Grown on Sapphire and Silicon

Here I will show the results for the XPS of f-PLD films on sapphire and silicon substrates. Much of the focus will remain on tungsten, oxygen, and when appropriate the sodium peaks of the fP4, fP5, fP8 and fP9 films post annealing. Results for all other films are shown in the Appendix.

Figure 3.16 shows the high-resolution scans for both the fP4 and fP5 films post annealing. Analysis of the high-resolution scan of the W 4f peak for the fP4 Pt-A as well

as for the fP5 Pt-A sample shows that the tungsten atoms in the sample primarily exhibit the +6 oxidation state. However, there are some small contributions from the +5 oxidation state of W in the XPS spectra. Since there is no sodium shown in the XPS survey scan for either the fP4 or the fP5 film the +5 oxidation state of W is most likely due to oxygen vacancies on the surface of the films.

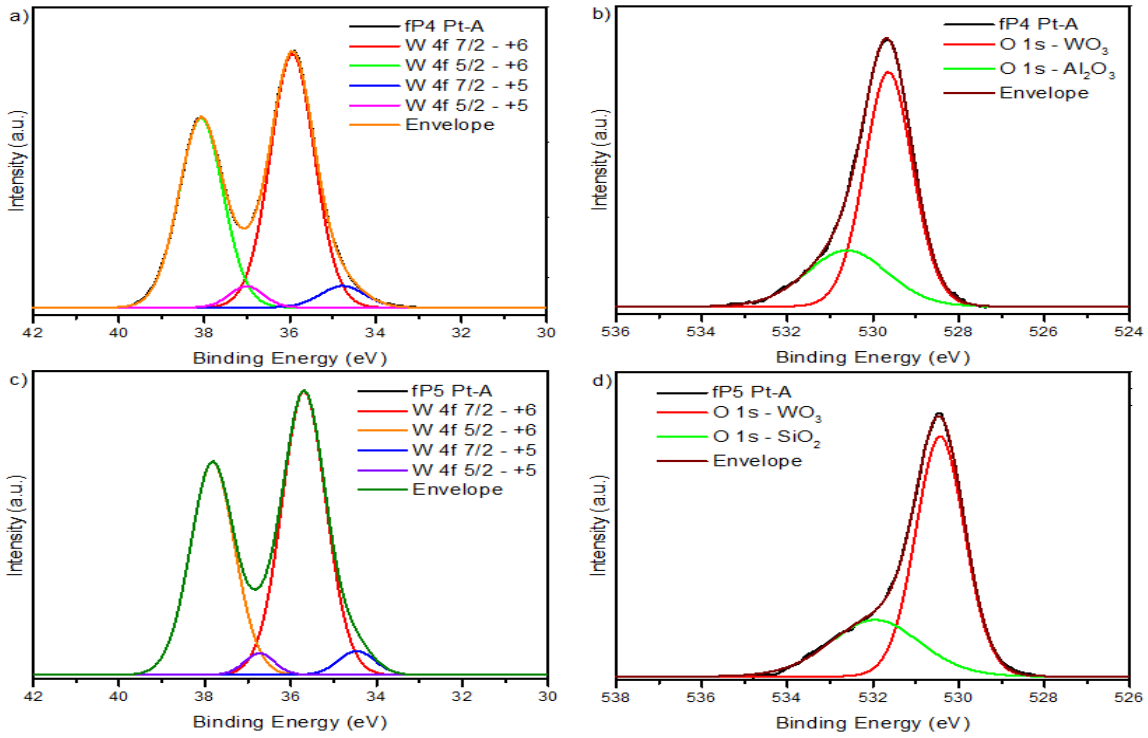

Figure 3.16: High resolution XPS for the fP4 Pt-A W 4f (a) and O 1s (b) and fP5 Pt-A W 4f (c) and O 1s (d).

Figure 3.17 shows the XPS high resolution scans for the fP8 Pt-A. Analysis of these scans shows the presence of sodium in the fP8 Pt-A thin films (11.03 at%). Since sodium is incorporated in the film, contributions from both the +6 and +5 oxidation state are expected in the W 4f high resolution XPS scans. After analysis, the contribution from the +5 oxidation state, while still much smaller than that of the +6 contribution, has a

larger area for the films containing sodium than for the films (fP4 and fP5) without any Na content. The +5 W oxidation state contributions are predominantly attributed to the donation of an electron from Na to W (5d states), upon Na insertion into the intercalation channels of the WO_3 structure of the thin films. This electron donation allows the oxidation state of some of the tungsten atoms to change from +6 to +5, while the remainder are changed due to oxygen vacancy formation at the surface of the thin film.

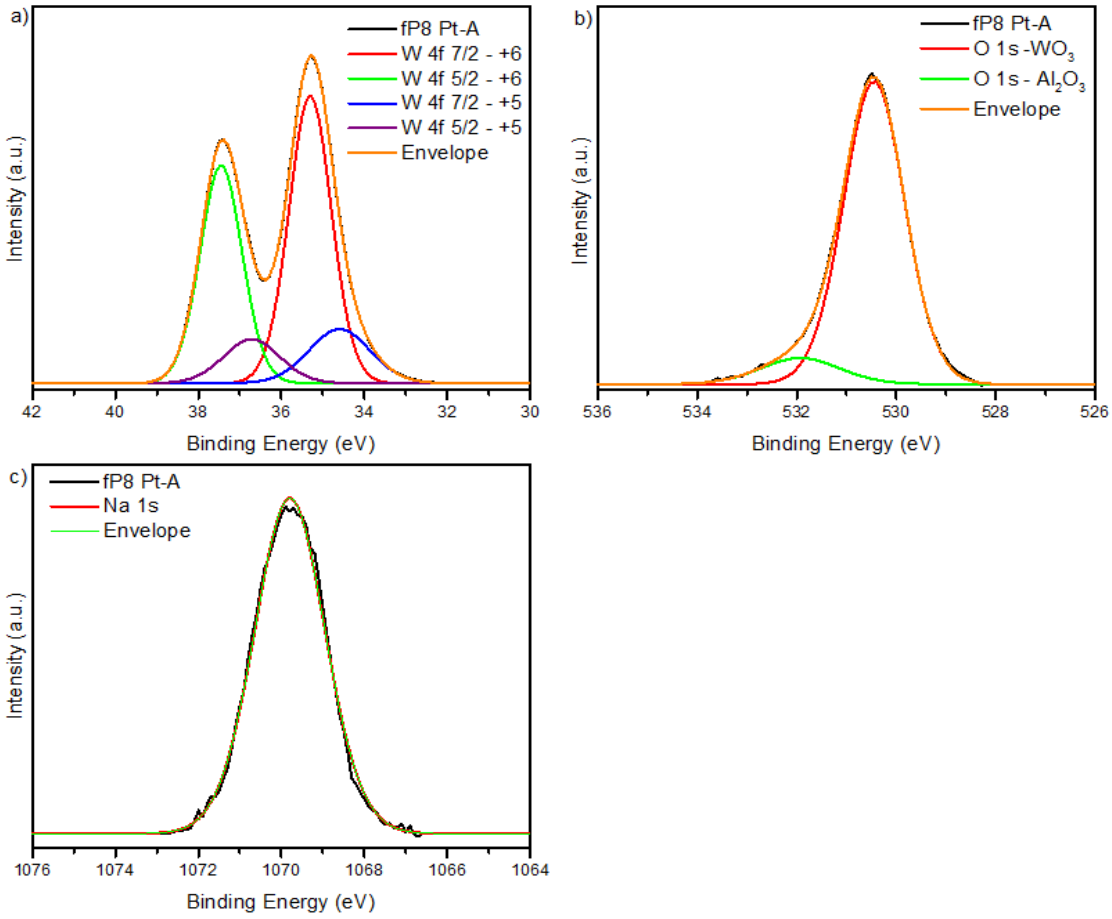

Figure 3.17: High resolution XPS for the fP8 Pt-A W 4f (a), O 1s (b), and Na 1s (c).

Figure 3.18 shows the high the XPS high resolution scans for the fP9 Pt-A. Analysis of the high resolution scans shows the presence of sodium in the fP9 Pt-A thin film (10.73 at%). The sodium content present in the fP9 film is similar to that of the fP8 film with contributions from the +6 and +5 oxidation states, which shows a larger contribution from the +5 oxidation state than in the case of WO_3 films.

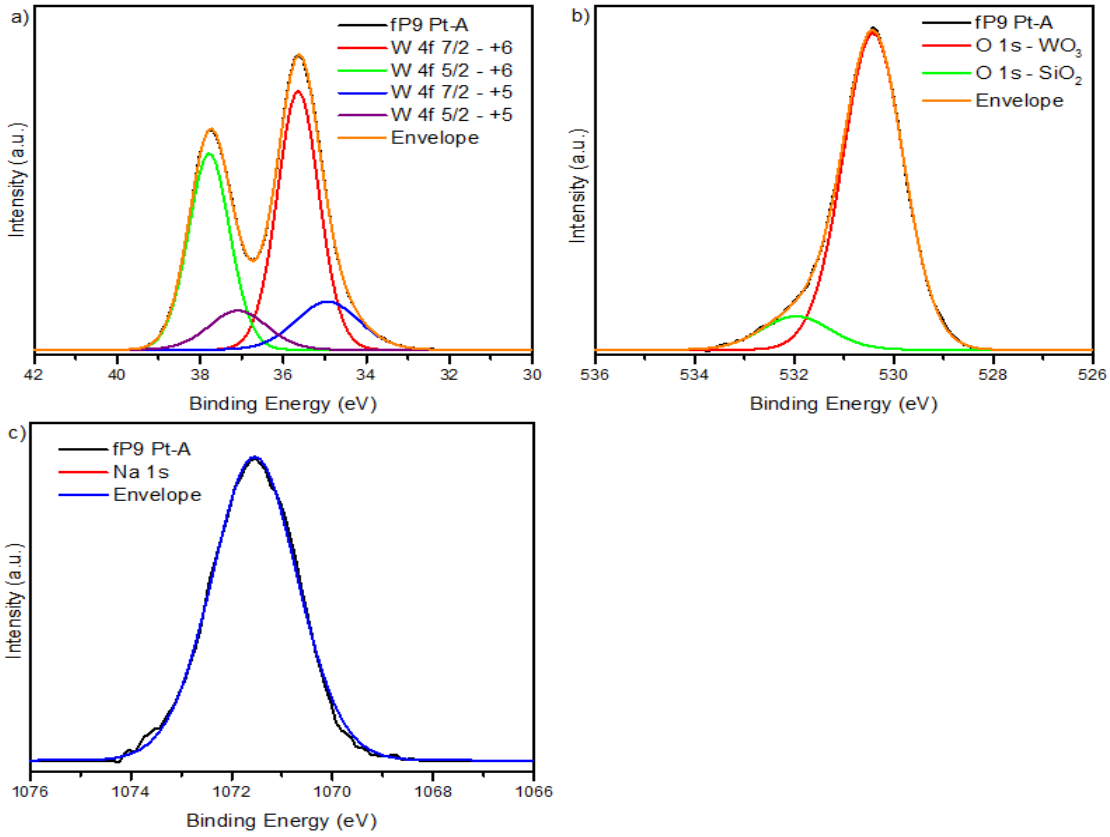

Figure 3.18: High resolution XPS data for the fP9 Pt-A W 4f (a), O 1s (b) and Na 1s (c).

Atomic Force Microscopy of Tungsten Oxide Thin Films Grown on Sapphire and Silicon

AFM was performed on the post annealed fP4, fP5, fP8, and fP9 films. Figure 3.19 shows the 3-dimensional AFM images of the fP4, fP5, fP8, and fP9 thin films; the 2-

dimensional AFM images of the same films can be found in the appendix. Both the 3-dimensional as well as the 2-dimensional AFM images for the fP4 and fP5 films show a relatively smooth surface that is marred by randomly dispersed sphere-like droplets. AFM images of the fP8 and fP9 films show a considerably rougher surface primarily composed of tower-like structures. However, the fP8 and fP9 films also show rod-like crystals growing on the smooth surfaces between high relief structures, which are consistent with the SEM images obtained for these films. Since these structures can only be seen in the Na_xWO_3 films the rod-like crystals are a result of lattice distortions caused by sodium insertion in these samples.

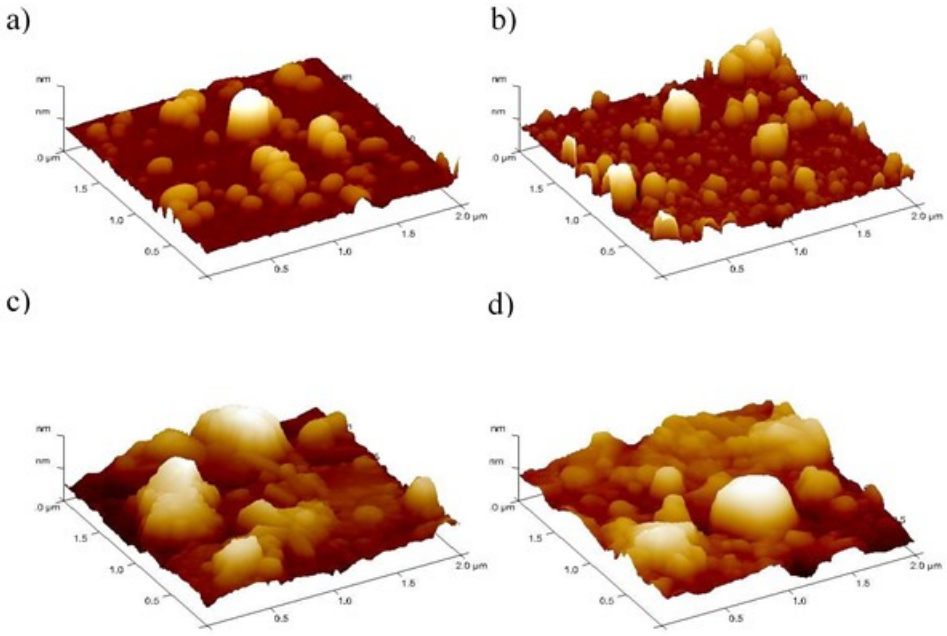

Figure 3.19: AFM images of the fP4 Pt-A (a), fP5 Pt-A (b), fP8 Pt-A (c), and the fP9 Pt-A (d) thin films.

Information on the texture of the film surface was obtained by the R_{rms} or surface roughness values, which were determined from the AFM 2d images. From these

measurements, I find that the R_{rms} values for the films deposited on sapphire are higher for both the WO_3 and Na_xWO_3 thin films, corresponding to higher surface area to volume ratios, than for the films deposited on Si, the reader is referred to the Appendix for these results. Interestingly, the Na_xWO_3 thin films deposited either on sapphire or Si exhibit more surface roughness than the WO_3 thin films. Since catalysis occurs on the surface of the material I would expect the sample with the larger roughness values to be more suitable for catalysis applications. Increased surface roughness values for films grown on sapphire are likely due to several factors including the surface morphology of the substrate. Surface morphology of pristine silicon substrates, as examined by SEM, exhibits a smooth surface, however, the sapphire substrates show a rougher surface than the silicon substrates. The rough surface of the sapphire likely leads to the increased roughness of films fabricated on this material.[49]

Overall Discussion

Films grown using n-PLD and f-PLD on glass substrates have high sodium contents due to sodium diffusion at the film interface during deposition as well as annealing. The presence of sodium is supported by the presence of multiple phases (triclinic, orthorhombic, monoclinic, and in cases having the greatest Na content, hexagonal) in the XRD data as well as the presence of Raman modes that are characteristic of tungsten bronze phases in the 400-600 cm^{-1} region. Since the various tungsten bronze phases depend on the amount of intercalated sodium, it is evident that the sodium incorporation is non-uniform, which is supported by XRD of the Na_xWO_3 target which shows multiple crystal structures. Finally, the most conclusive evidence of sodium

insertion appears from the XPS survey scan and high resolution scans of the W 4f and Na 1s peaks. All films grown on glass show significant contributions from the W 4f +5 oxidation states in the Na_xWO_3 thin films, thus providing evidence for tungsten bronze phases in agreement with the XRD data.

The films grown using f-PLD on sapphire and silicon substrates exhibit similar results to those obtained from the films on glass except for sodium content. Four films (fP2, fP3, fP4, and fP5) were grown using a monoclinic WO_3 target, however, evidence for multiple phases (monoclinic, orthorhombic, tetragonal, triclinic, hexagonal, and cubic) is found in XRD, XPS, and Raman spectroscopy for these films. These phases are likely locked into the material by lattice distortion caused by oxygen deficiencies. Films (fP6, fP7, fP8, and fP9) that were grown using the Na_xWO_3 target also have similar characteristics to the ones grown using the WO_3 target using f-PLD. One important thing to note is that these films show a larger amount of the +5 oxidation state W than do the fP2-fP5 films, which points to distortions caused by oxygen deficiencies providing for growth of metastable phases as well as tungsten bronzes due to sodium insertion.

CONCLUSIONS

SEM and HIM imaging of thin film samples reveal that samples fabricated using f-PLD on glass have a 3-dimensional, nanostructured morphology that the n-PLD technique is currently incapable of producing. Results for the SEM made on f-PLD samples of films grown on silicon and sapphire substrates share similar morphological traits to those obtained from the f-PLD film grown on glass with one exception: Films grown from the Na_xWO_3 target also show signs of smaller rod-like crystals forming on both the low and high relief areas of the films, which is also supported by AFM images of the fP8 and fP9 films. Results obtained from visual inspection of SEM images as well as the R_{rms} values obtained from the AFM images indicate that f-PLD films grown on sapphire produce films with greater surface area to volume ratios than n-PLD films grown on the same types of substrates.

Characteristic vibrational modes of the WO_3 polymorphs are present in the Raman spectra, which are dominated by the apical O vibration in the WO_6 octahedra (700-850 cm^{-1} region) as well as several contributions from the O-W-O bending modes in the (150-350 cm^{-1} region). Raman vibrational modes are also present in the 400- 600 cm^{-1} region, which are attributable to both tungsten bronze materials as well as metastable polymorphs of WO_3 due to oxygen deficencies The presence of the tungsten bronze and polymorph phases lead to changes in the electrical, chemical, and physical properties of WO_3, which could make these materials more suitable for applications in photocatalysis, batteries, and fuel cells. Further study will need to be conducted to determine what

changes have occurred in the material's properties due to these mixed phases in the tungsten oxide thin films.

XRD provides more evidence for the presence of mixed phase films which arise from two mechanisms, regardless of the substrate material, primarily involving distortion of the interconnectivity of the WO_6 octahedrons that are the basic building units of the tungsten oxide polymorphs. The two mechanisms responsible for these distortions are intercalated Na^+ ions as well as oxygen deficiencies throughout the film. Evidence for multiple phases can also be inferred from the XPS data, due to contributions from the +5 oxidation state of W in the thin films. The changes in oxidation state could occur during laser ablation, but is most likely due to oxygen vacancies on the surface of the WO_3 thin films or due to Na incorporation in the Na_xWO_3thin films. From the results obtained in this study, I conclude that films grown using the f-PLD technique would provide a more suitable material for photocatalysis due to the increased surface roughness, especially films grown on sapphire since they display the highest surface roughness values as determined by analysis of AFM data.

REFERENCES

(1) Kemdeo, S. M.; Sapkal, V. S.; Chaudhari, G. N. *Bull. Chem. React. Eng. Catal.* **2010**, *5* (1), 39–49.

(2) Al-Kuhaili, M. F.; Durrani, S. M. A.; Bakhtiari, I. A. *Appl. Phys. Mater. Sci. Process.* **2010**, *98* (3), 609–615.

(3) Warren, B. E. *X-Ray Diffraction*; Courier Corporation, 2012.

(4) Eason, R. *Pulsed Laser Deposition of Thin Films: Applications-Led Growth of Functional Materials*; John Wiley & Sons, 2007.

(5) Castillejo, M.; de Nalda, R.; Oujia, M.; Sanz, M. *AIP Conf. Proc.* **2010**, *1278* (1), 303–311.

(6) Wang, K. Laser Based Fabrication of Graphene http://www.intechopen.com/books/advances-in-graphene-science/laser-based-fabrication-of-graphene (accessed Apr 20, 2017).

(7) Millon, E.; Albert, O.; Loulergue, J. C.; Etchepare, J.; Hulin, D.; Seiler, W.; Perriere, J. J. Appl. Phys. 2000, 88 (11), 6937.

(8) Millon, E.; Perrière, J.; Défourneau, R. M.; Défourneau, D.; Albert, O.; Etchepare, J. *Appl. Phys. A* **2003**, *77* (1), 73–80.

(9) Chichkov, B. N.; Momma, C.; Nolte, S.; von Alvensleben, F.; Tünnermann, A. *Appl. Phys. Mater. Sci. Process.* **1996**, *63* (2), 109–115.

(10) Dominguez, J. E.; Pan, X. Q.; Fu, L.; Van Rompay, P. A.; Zhang, Z.; Nees, J. A.; Pronko, P. P. *J. Appl. Phys.* **2002**, *91* (3), 1060.

(11) Shirk, M. D.; Molian, P. A. *J. Laser Appl.* **1998**, *10* (1), 18–28.

(12) Wolfe, D. b.; Ashcom, J. b.; Hwang, J. c.; Schaffer, C. b.; Mazur, E.; Whitesides, G. m. *Adv. Mater.* **2003**, *15* (1), 62–65.

(13) Giridhar, M. S.; Seong, K.; Schülzgen, A.; Khulbe, P.; Peyghambarian, N.; Mansuripur, M. *Appl. Opt.* **2004**, *43* (23), 4584–4589.

(14) Darby, M. Femtosecond Pulsed Laser Deposition, University of Southampton, 2009.

(15) Gattass, R. R.; Mazur, E. *Nat. Photonics* **2008**, *2* (4), 219–225.

(16) Huang, K.; Pan, Q.; Yang, F.; Ni, S.; Wei, X.; He, D. *J. Phys. Appl. Phys.* **2008**, *41* (15), 155417.

(17) Gao, T.; Jelle, B. P. *J. Phys. Chem. C* **2013**, *117* (26), 13753–13761.

(18) Vijayalakshmi, R.; Jayachandran, M.; Trivedi, D.; Sanjeeviraja, C. *Synth. React. Inorg. Met.-Org. Nano-Met. Chem.* **2006**, *36* (1), 89–94.

(19) Garg, A.; Leake, J. A.; Barber, Z. H. *J. Phys. Appl. Phys.* **2000**, *33* (9), 1048.

(20) Wen, Z.; Wu, W.; Liu, Z.; Zhang, H.; Li, J.; Chen, J. *Phys. Chem. Chem. Phys. PCCP* **2013**, *15* (18), 6773–6778.

(21) Bamwenda, G. R.; Arakawa, H. *Appl. Catal. Gen.* **2001**, *210* (1–2), 181–191.

(22) Zhao, Z.-G.; Miyauchi, M. *Angew. Chem.* **2008**, *120* (37), 7159–7163.

(23) Wang, L.; Zhan, J.; Fan, W.; Cui, G.; Sun, H.; Zhuo, L.; Zhao, X.; Tang, B. *Chem. Commun.* **2009**, *46* (46), 8833–8835.

(24) Rao, M. C. *J. Non-Oxide Glas.* **2013**, *5* (1), 1–8.

(25) Richard, A. P.; Edwards, D. D. *MRS Online Proc. Libr. Arch.* **2002**, *756*.

(26) Mamak, M.; Choi, S. Y.; Stadler, U.; Dolbec, R.; Boulos, M.; Petrov, S. *J. Mater. Chem.* **2010**, *20* (44), 9855–9857.

(27) Tungsten»tungsten trioxide [WebElements Periodic Table] https://www.webelements.com/compounds/tungsten/tungsten_trioxide.html (accessed Apr 20, 2017).

(28) LeGore, L. J.; Lad, R. J.; Moulzolf, S. C.; Vetelino, J. F.; Frederick, B. G.; Kenik, E. A. *Thin Solid Films* **2002**, *406* (1–2), 79–86.

(29) Jiao, Z.; Wang, J.; Ke, L.; Sun, X. W.; Demir, H. V. *ACS Appl. Mater. Interfaces* **2011**, *3* (2), 229–236.

(30) Goldstein, J.; Newbury, D. E.; Echlin, P.; Joy, D. C.; Jr, A. D. R.; Lyman, C. E.; Fiori, C.; Lifshin, E. *Scanning Electron Microscopy and X-Ray Microanalysis: A Text for Biologists, Materials Scientists, and Geologists*; Springer Science & Business Media, 2012.

(31) Havancsak, K. TECHNOORG - LINDA http://www.technoorg.hu/news-and-events/articles/high-resolution-scanning-electron-microscopy-1/ (accessed Apr 20, 2017).

(32) Ward, B. W.; Notte, J. A.; Econumou, N. P. *J. Vac. Sci. Technol. B Microelectron. Nanometer Struct. Process. Meas. Phenom.* **2006**, *24* (6), 2871–2874.

(33) x-ray diffraction http://encyclopedia2.thefreedictionary.com/x-ray+diffraction (accessed Apr 20, 2017).

(34) Hahn, D. University of Florida February 2007.

(35) *Wikipedia*; 2017.

(36) Chusuei, C. C.; Goodman, D. W. In *Encyclopedia of Physical Science and Technology (Third Edition)*; Meyers, R. A., Ed.; Academic Press: New York, 2003; pp 921–938.

(37) Horton, J. Dr. J. Hugh Horton » Research Projects http://faculty.chem.queensu.ca/people/faculty/horton/research.html (accessed Apr 20, 2017).

(38) Eaton, P.; West, P. *Atomic Force Microscopy*; Oxford University Press, 2010.

(39) D'Antò, V.; Rongo, R.; Ametrano, G.; Spagnuolo, G.; Manzo, P.; Martina, R.; Paduano, S.; Valletta, R. *Angle Orthod.* **2012**, *82* (5), 922–928.

(40) Dey, S.; Anderson, S. T.; Mayanovic, R. A.; Sakidja, R.; Landskron, K.; Kokoszka, B.; Mandal, M.; Wang, Z. *Nanoscale* **2016**, *8* (5), 2937–2943.

(41) da Silva, K. P.; Paraguassu, W.; Maczka, M.; Filho, A. G. S.; Freire, P. T. C.; Filho, J. M.; Hanuza, J. *J. Raman Spectrosc.* **2011**, *42* (3), 474–481.

(42) Lee, S.-H.; Cheong, H. M.; Tracy, C. E.; Mascarenhas, A.; Benson, D. K.; Deb, S. K. *Electrochimica Acta* **1999**, *44* (18), 3111–3115.

(43) Scott, J. F.; Leheny, R. F.; Remeika, J. P.; Sweedler, A. R. *Phys. Rev. B* **1970**, *2* (10), 3883–3887.

(44) Hollinger, G.; Minh Duc, T.; Deneuville, A. *Phys. Rev. Lett.* **1976**, *37* (23), 1564–1567.

(45) Serra, J.; González, P.; Liste, S.; Serra, C.; Chiussi, S.; León, B.; Pérez-Amor, M.; Ylänen, H. O.; Hupa, M. *J. Non-Cryst. Solids* **2003**, *332* (1–3), 20–27.

(46) Jeong, J. I.; Hong, J. H.; Moon, J. H.; Kang, J.-S.; Fukuda, Y. *J. Appl. Phys.* **1996**, *79* (12), 9343.

(47) Lethy, K. J.; Beena, D.; Kumar, R. V.; Pillai, V. P. M.; Ganesan, V.; Sathe, V.; Phase, D. M. *Appl. Phys. A* **2008**, *91* (4), 637–649.

(48) Mitsugi, F.; Hiraiwa, E.; Ikegami, T.; Ebihara, K.; Thareja, R. K. *Jpn. J. Appl. Phys.* **2002**, *41* (8R), 5372.

(49) Yamauchi, R.; Hamasaki, Y.; Shibuya, T.; Saito, A.; Tsuchimine, N.; Koyama, K.; Matsuda, A.; Yoshimoto, M. *Sci. Rep.* **2015**, *5*, 14385.

APPENDIX

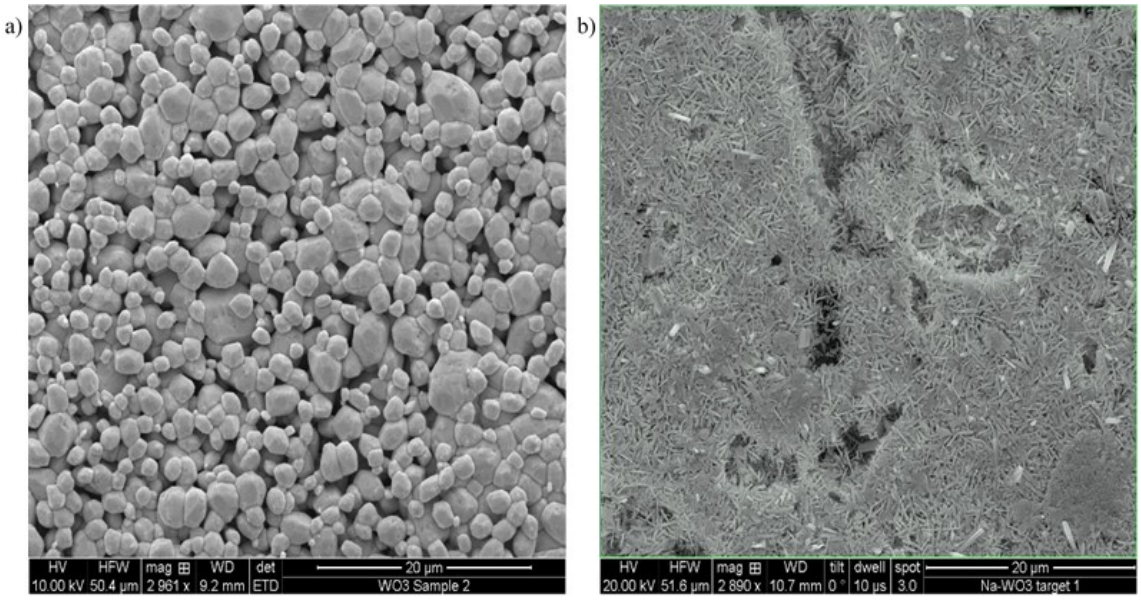

SEM of the WO_3 target post annealing (a) and the Na_xWO3 targets (b).

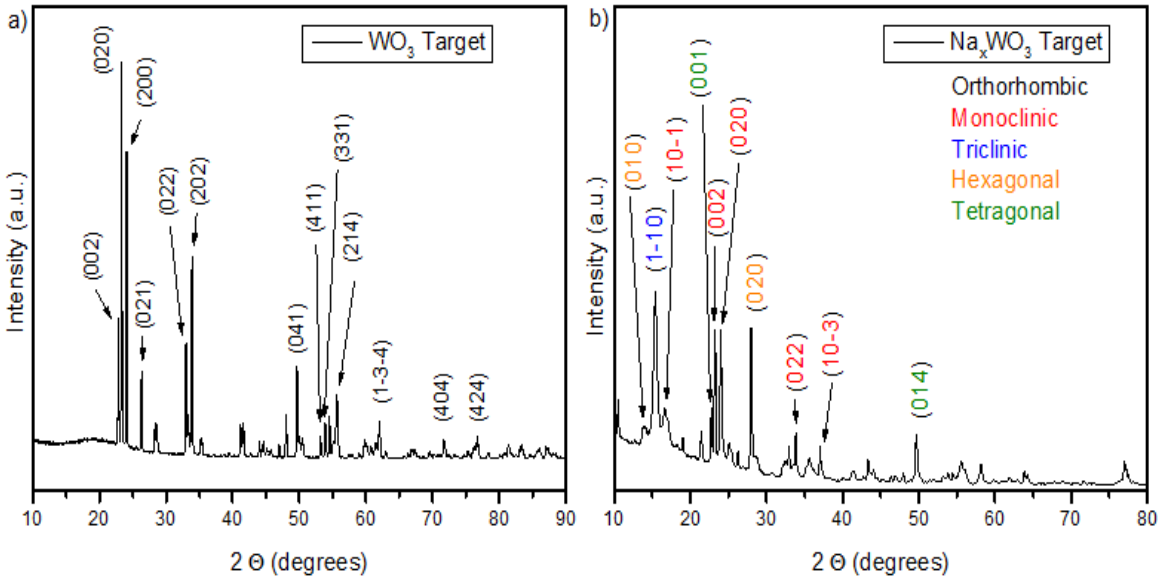

XRD of the WO_3 target (a) and the Na_xWO_3 target (b).

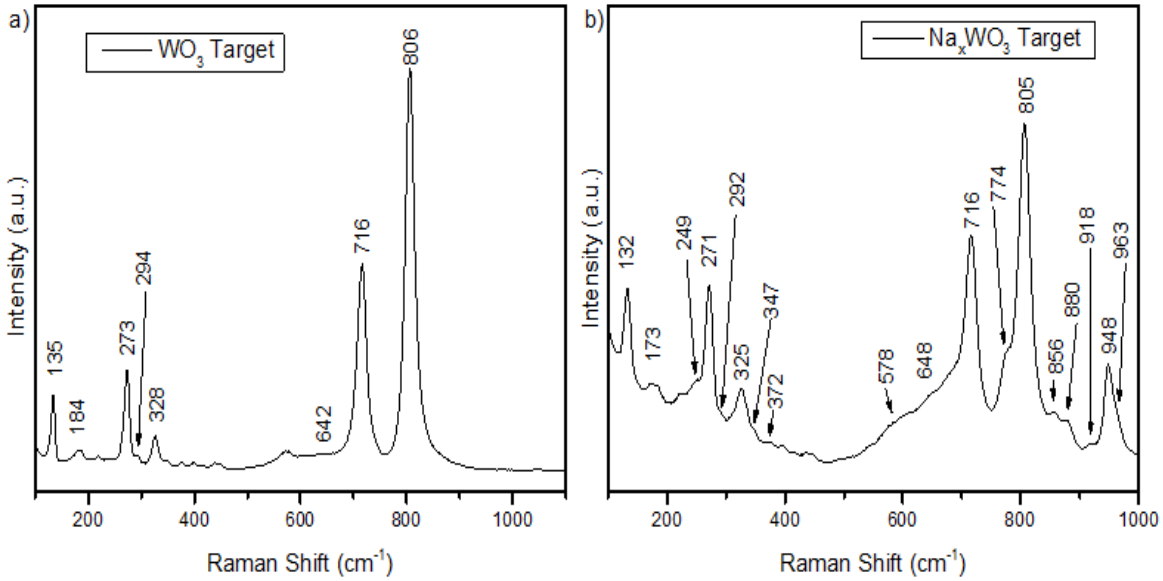

Raman spectroscopy of (a) the WO_3 target and the Na_xWO_3 target (b).

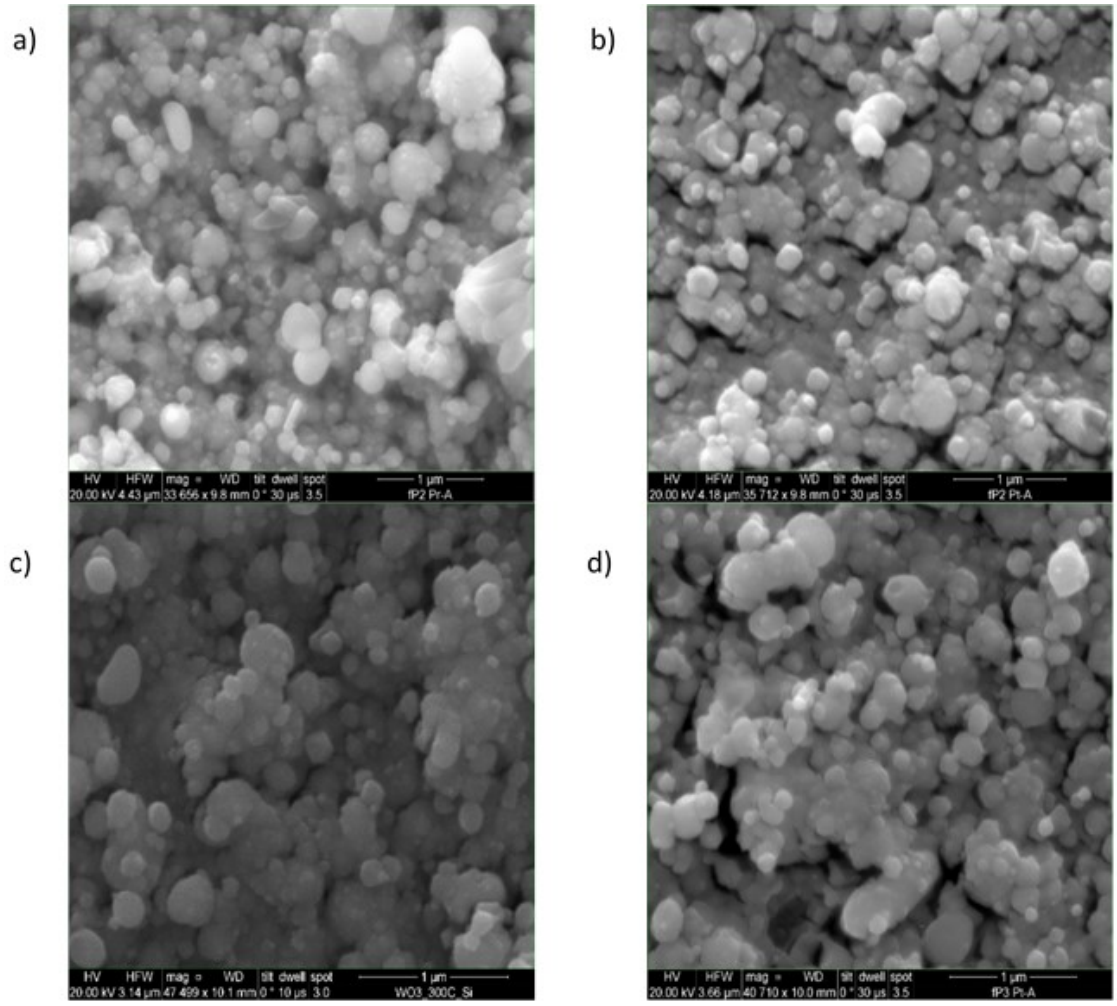

SEM micrographs of the fP2 (a) and fP3 films (c) prior annealing and fP2 (b) and fP3 (d) post annealing.

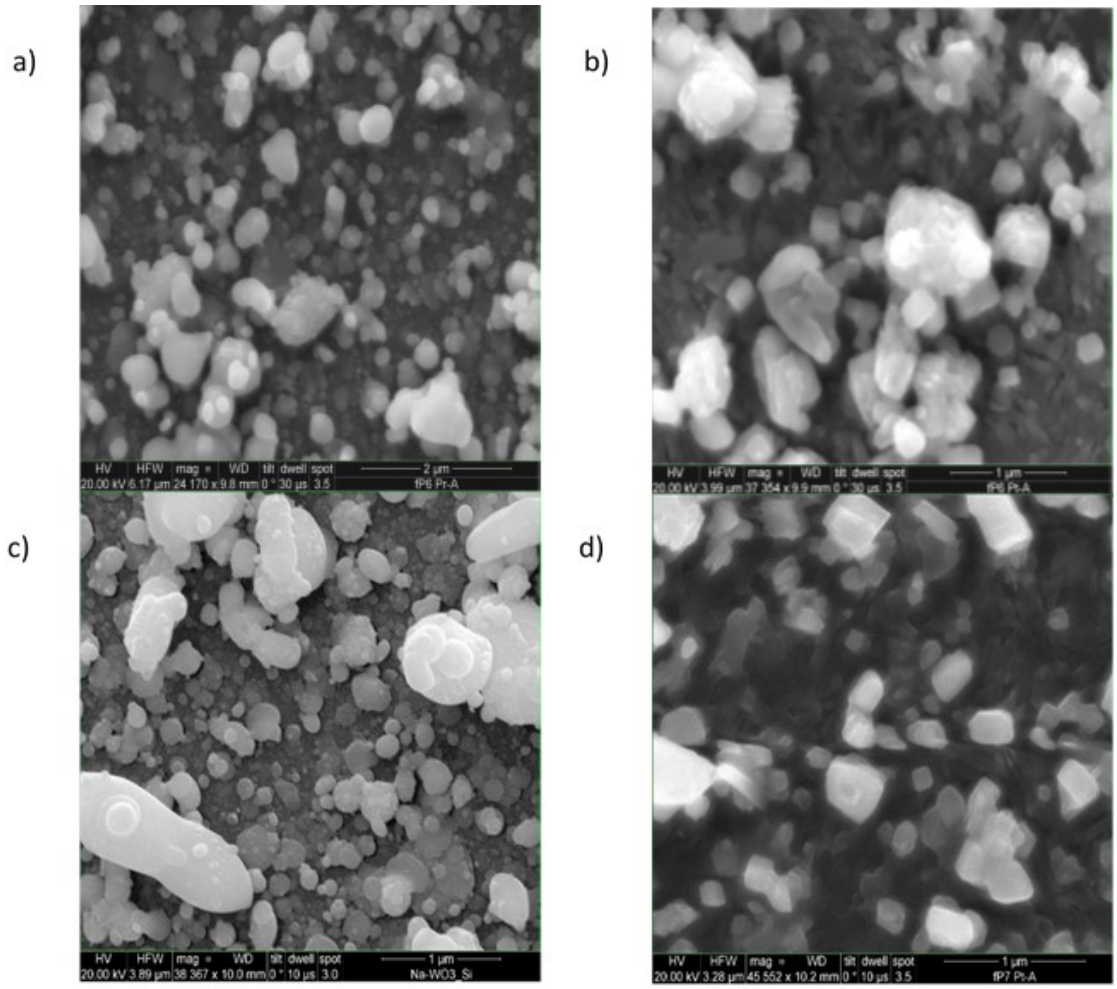

SEM micrographs of the fP6 (a) and fP7 films (c) prior annealing and fP6 (b) and fP7 (d) post annealing.

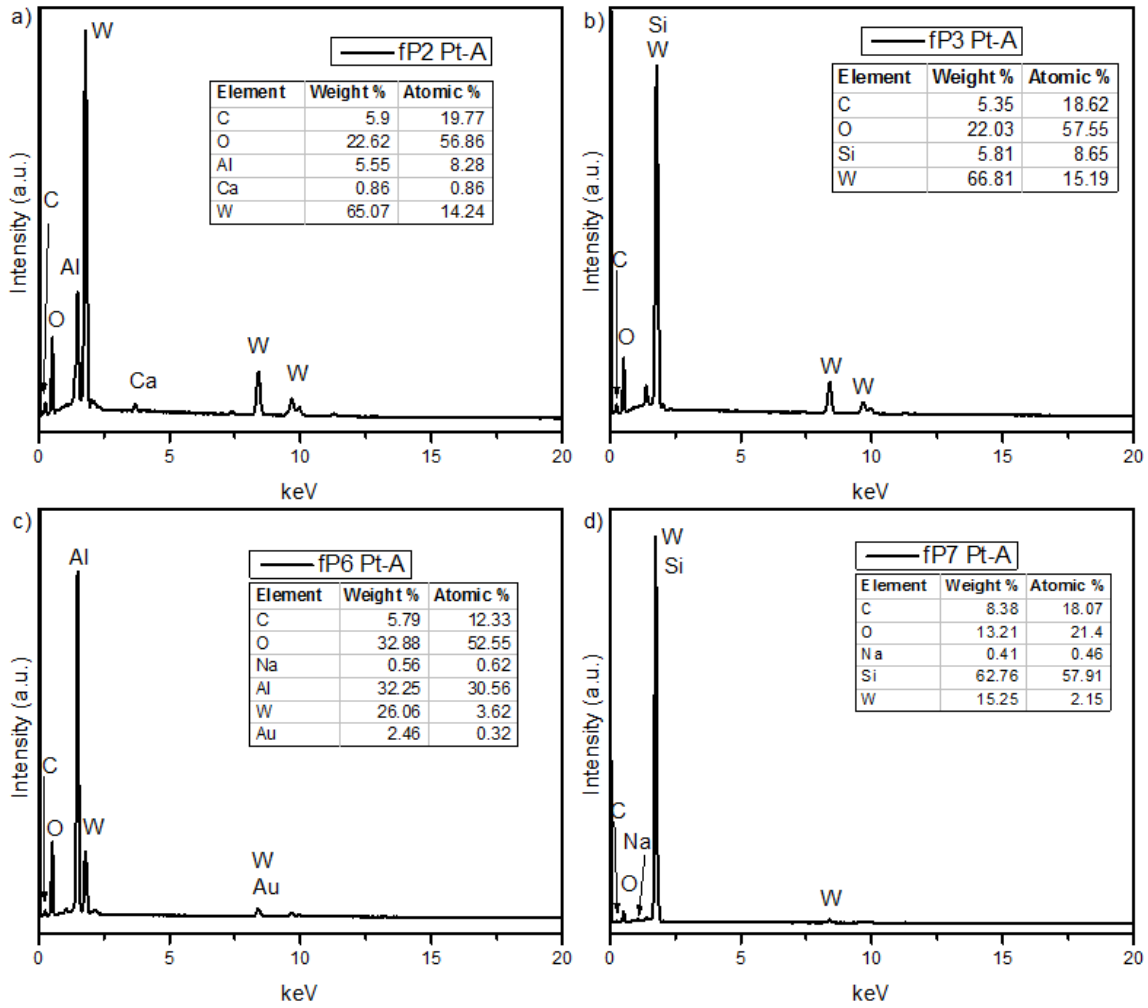

EDX on the fP2 (a), fP3 (b), fP6 (c), and fP7 (d) films post annealing.

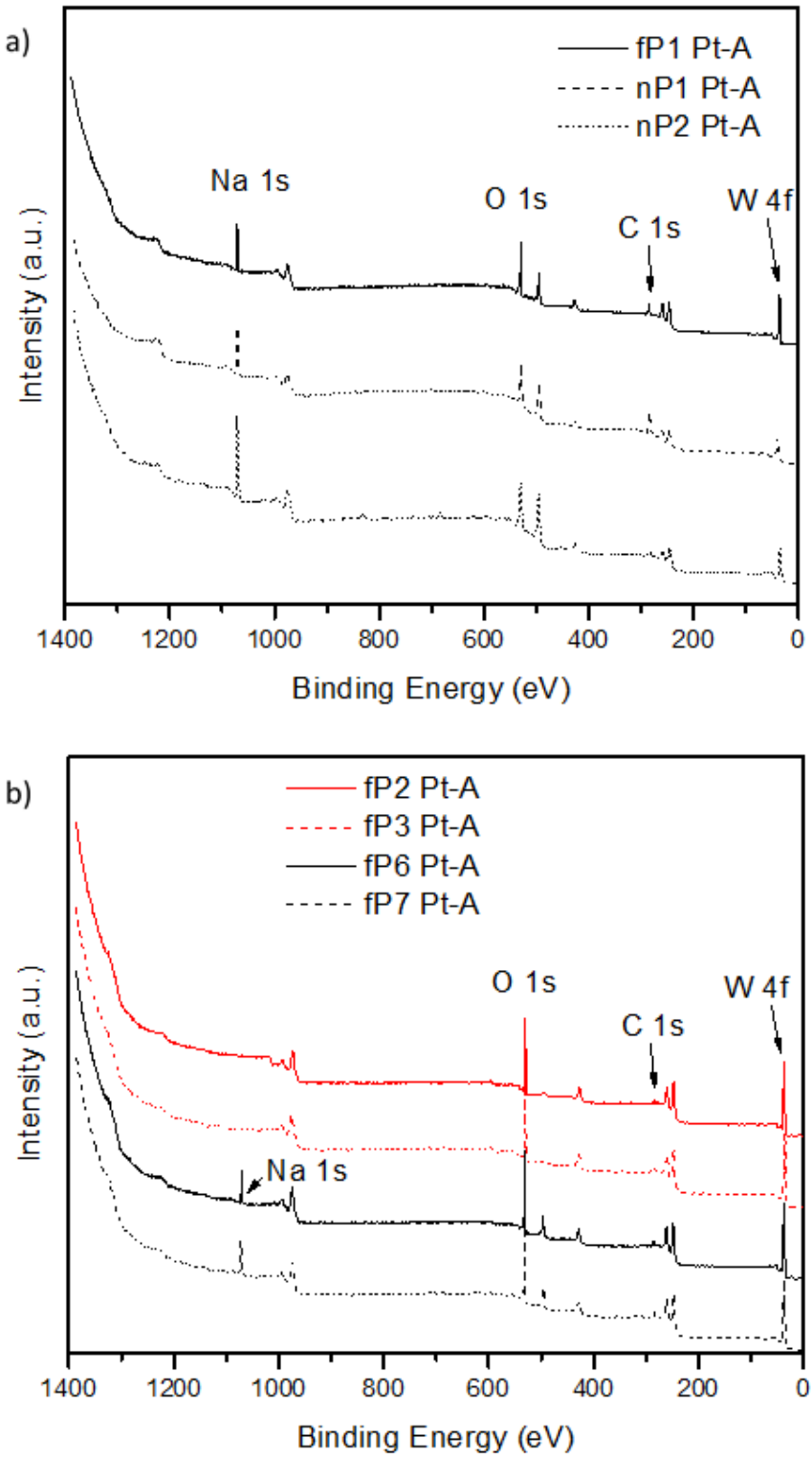

XPS survey scans for films grown on glass (a) and XPS survey scans for the films grown on sapphire and silicon substrates (b).

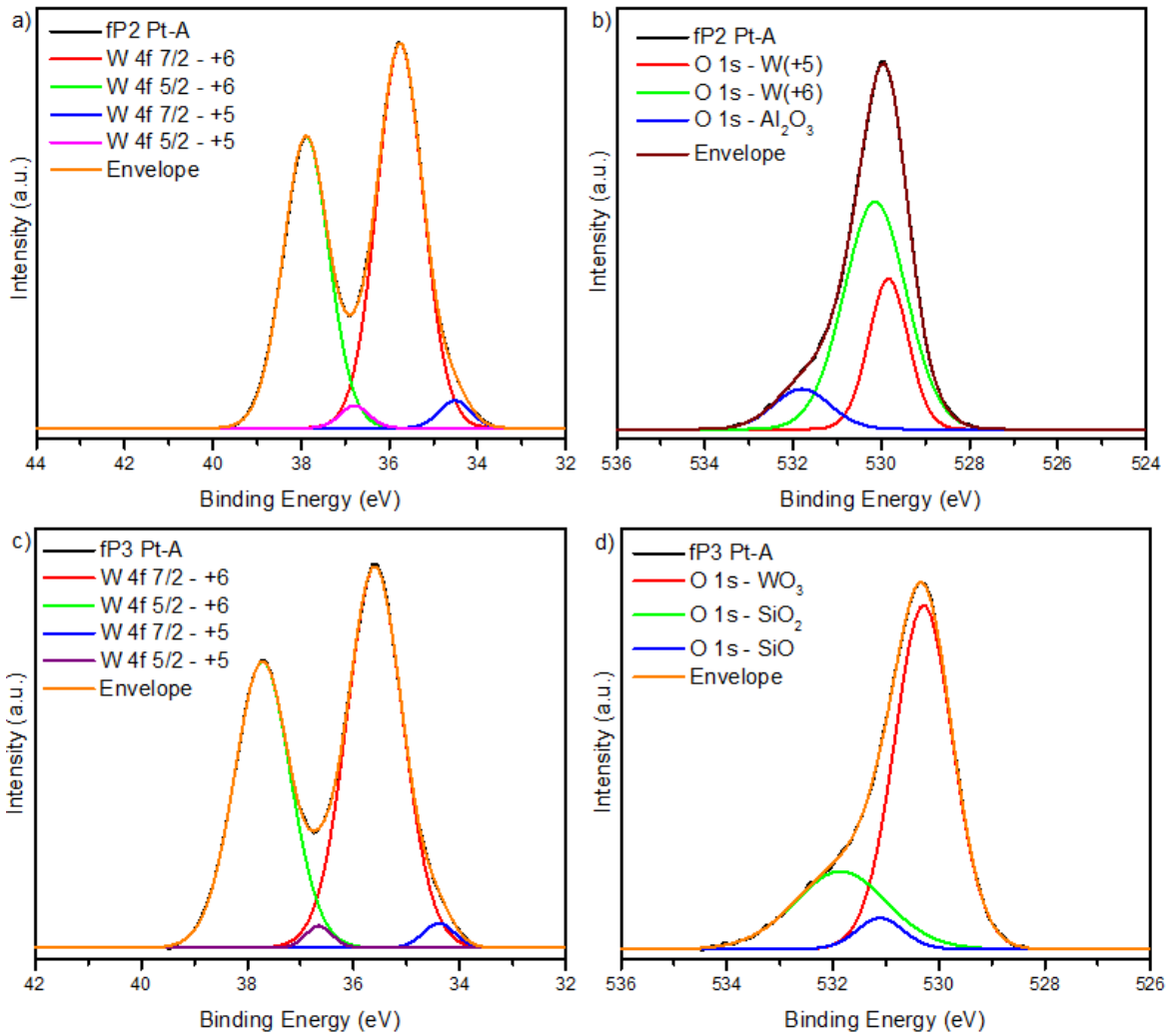

High resolution XPS for the fP4 Pt-A W 4f (a) and O 1s (b) and fP5 Pt-A W 4f (c) and O 1s (d).

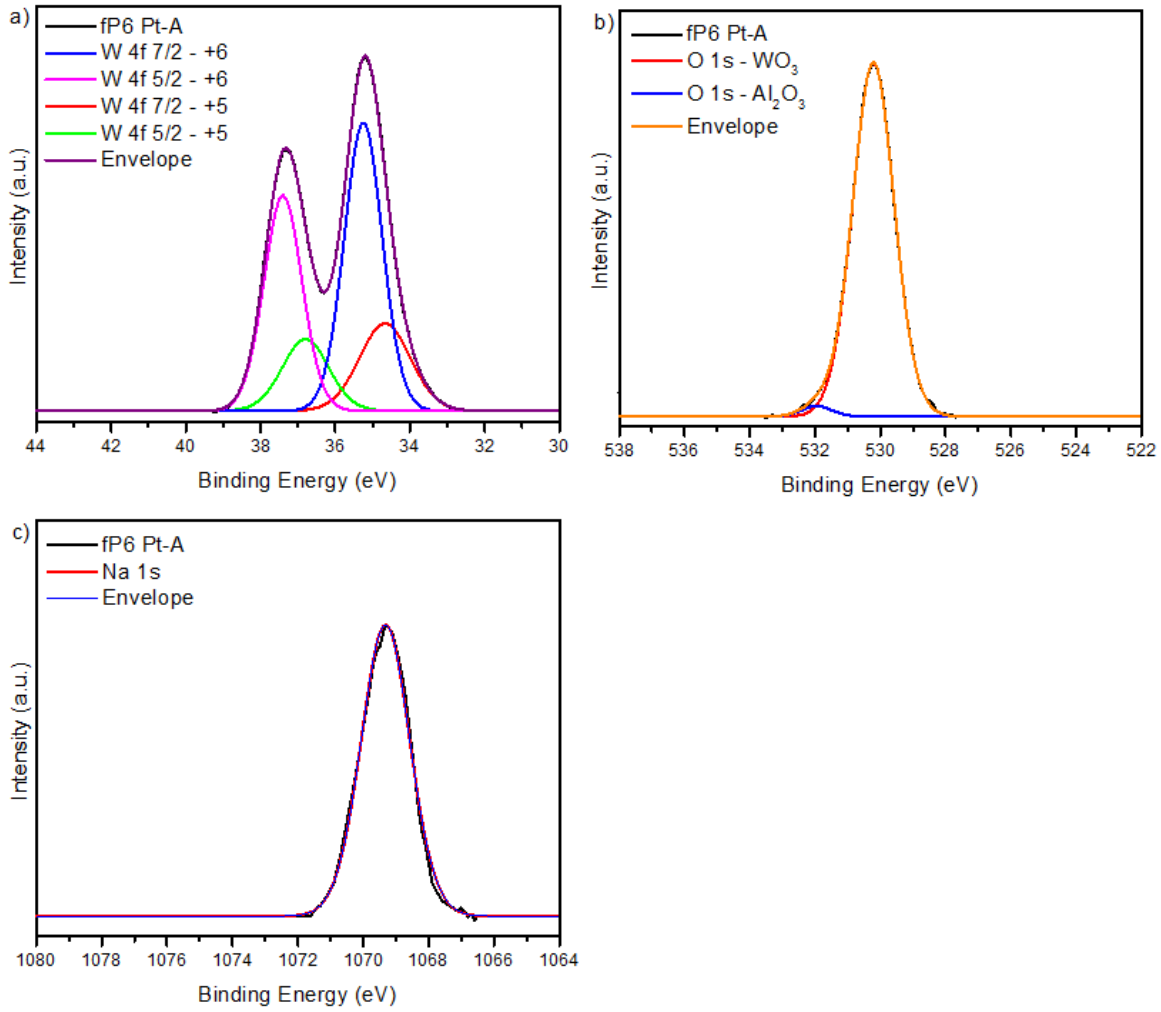

High resolution XPS for the fP6 Pt-A W 4f (a), O 1s (b), and Na 1s (c).

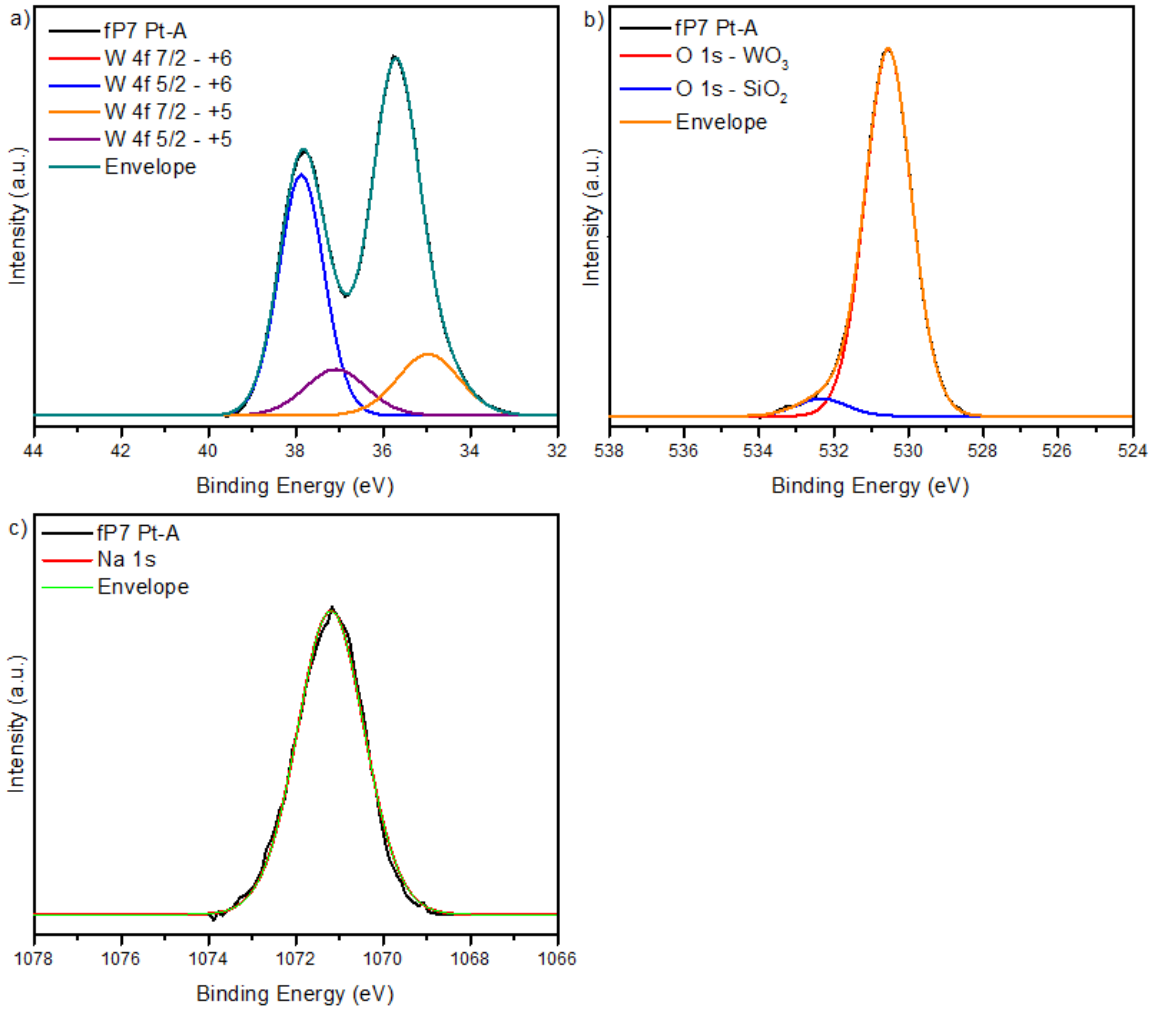

High resolution XPS for the fP7 Pt-A W 4f (a), O 1s (b), and Na 1s (c).

XPS survey scan information for relevant peaks from fP1 – fP5 as well as nP1 and nP2 samples post annealing.

	Element	Position (eV)	FWHM (eV)	Area (eV)	At% Conc.
fP1 Pt-A	Na 1s	1071.44	1.86	2263.03	15.53
	O 1s	529.94	1.75	3233.74	64.51
	W 4f	36.44	1.75	3347.43	19.97
nP1 Pt-A	Na 1s	1070.40	2.43	2825.61	22.27
	O 1s	529.90	2.71	2768.27	63.43
	W 4f	39.90	3.83	2087.80	14.30
nP2 Pt-A	Na 1s	1070.40	2.43	2825.61	22.27
	O 1s	529.90	2.71	2768.27	63.43
	W 4f	39.90	3.83	2087.80	14.30
fP2 Pt-A	O 1s	530.51	1.69	6091.45	73.50
	W 4f	36.51	1.41	7346.14	26.50
fP3 Pt-A	O 1s	530.51	1.64	6857.56	72.57
	W 4f	35.51	1.51	8668.46	27.43
fP4 Pt-A	O 1s	530.30	1.64	3650.20	73.48
	W 4f	36.80	1.48	4406.80	26.52
fP5 Pt-A	O 1s	530.30	1.65	7484.57	74.52
	W 4f	35.30	1.50	8557.78	25.48

Peak positions for Na 1s, O1s and W 4f peaks for the fP6 – fP9 films post annealing obtained from the XPS survey scan.

	Element	Position (eV)	FWHM (eV)	Area (eV)	At% Conc.
fP6 Pt-A	Na 1s	1070.51	1.84	2663.59	9.78
	O 1s	531.51	1.66	6122.44	65.34
	W 4f	36.51	1.58	7799.50	24.89
fP6 Pt-A	Na 1s	1072.01	1.89	2802.54	10.53
	O 1s	531.01	1.66	5817.78	63.58
	W 4f	36.51	1.70	7921.85	25.88
fP8 Pt-A	Na 1s	1070.30	2.07	2502.40	11.03
	O 1s	530.30	1.73	5020.37	64.36
	W 4f	35.30	1.59	6419.90	24.61
fP9 Pt-A	Na 1s	1071.80	2.06	3164.72	10.73
	O 1s	530.80	1.69	6547.29	66.80
	W 4f	35.8	1.54	7646.23	22.46

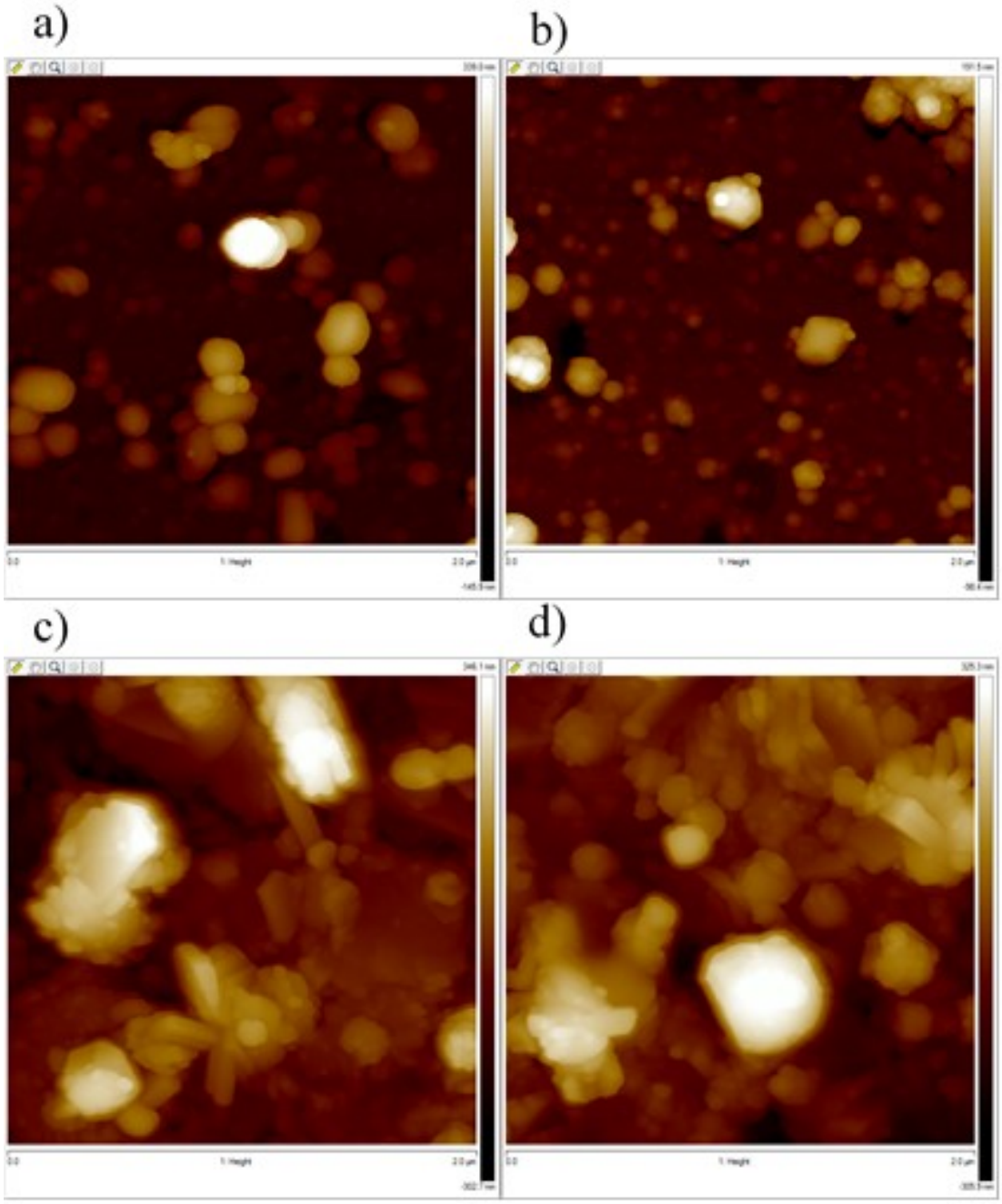

Two-dimensional AFM of fP4 (a), fP5 (b), fP8 (c) and fP9 (d).

Surface roughness values obtained for selected films.

Film	Surface Roughness (nm)
fP4 Pt-A	62.9
fP5 Pt-A	35.6
fP8 Pt-A	109
fP9 Pt-A	98.3